Hierarchical Heterogeneities in Spatio-Temporal Dynamics of the Cytoplasm

Conrad Möckel,[1,2,3,*] Abin Biswas,[1,2,4] Simone Reber,[4,5]
Aleksei Chechkin,[6,7,8] Vasily Zaburdaev,[2,3] and Jochen Guck[1,2,3,**]

[1] *Max Planck Institute for the Science of Light, 91058 Erlangen, Germany*
[2] *Max-Planck-Zentrum für Physik und Medizin, 91054 Erlangen, Germany*
[3] *Friedrich-Alexander-Universität Erlangen-Nürnberg, 91058 Erlangen, Germany*
[4] *Max Planck Institute for Infection Biology, 10117 Berlin, Germany*
[5] *Berliner Hochschule für Technik, 13353 Berlin, Germany*
[6] *Wroclaw University of Science and Technology, 50-370 Wrocław, Poland*
[7] *University of Potsdam, 14476, Potsdam-Golm, Germany*
[8] *Max Planck Institute of Microstructure Physics, 06120 Halle (Saale), Germany*

(Dated: May 8, 2025)

Understanding of the dynamics inherent to biological matter is crucial for illuminating the physical mechanisms underlying cellular processes. In this study, we employ bright-field differential dynamic microscopy (DDM) to investigate density fluctuations inherent in a cell-free model of eukaryotic cytoplasm. Our measurements reveal subdiffusive fractional Brownian motion and non-Gaussian displacement distributions, highlighting cytoplasmic heterogeneity. We introduce an empirical model that combines fractional Brownian motion with an inverse Gaussian distribution of diffusivities to describe the observed non-Gaussianity. Validated through Monte Carlo simulations, this model allows us to estimate the fractional diffusivity and exponent effectively. By altering macromolecular composition, the addition of energy, and assembly of a cytoskeleton, we identify three independent mechanisms that result in similar fractional exponents yet distinct diffusivities. We find that energy addition leads to non-stationary dynamics, in contrast to the stationary behavior observed under passive conditions. Presence of microtubules introduces a secondary dynamical timescale, which we describe using a two-state fractional Brownian motion model to differentiate between cytosolic and microtubule network associated contributions. Our findings demonstrate the effectiveness of DDM as a label-free tool for quantifying viscoelastic and heterogeneous properties of the cytoplasm and provide insights into how physical and biochemical factors, including cytoskeletal organization, govern subcellular dynamics.

Keywords: differential dynamic microscopy, fractional Brownian motion, anomalous diffusion, subcellular viscoelasticity, physical properties of the cytoplasm

I. INTRODUCTION

The cytoplasm is a highly dynamic and heterogeneous environment, comprising a complex mixture of macromolecules, organelles, cytoskeletal networks, and phase-separated compartments [1–3]. The behavior of these components is governed by physical properties such as local crowdedness, viscosity, and density, as well as various statistical processes [4]. Collectively, these factors influence diffusion modes, affect interactions between specific macromolecular species, and ultimately drive biological functions [5–9]. Despite the adaptability of living systems to external cues [10–12], the precise mechanisms governing cytoplasmic dynamics, such as anomalous diffusion [13], are not yet fully understood. Achieving a comprehensive understanding of these dynamics is crucial for illuminating a wide range of biological phenomena, including self-organization, signaling, cell division, migration, homeostasis, disease progression, and morphogenesis [2, 14].

While of fundamental interest, characterizing cytoplasmic dynamics poses significant challenges. Standard techniques, such as atomic force microscopy (AFM) [15], active and passive microrheology via single-particle tracking (PT) [16–18], fluorescence correlation spectroscopy (FCS) [19–21], and micropipette aspiration [22, 23], provide invaluable insights, advancing and shaping our notion of the physical cytoplasm. However, these methods are typically limited by their localized measurements, introduction of extrinsic labels, or reliance on theoretical models to infer subcellular properties from global cellular observations [24, 25]. In recent years, differential dynamic microscopy (DDM) has emerged as a complementary, label-free technique for inferring the microrheological properties of samples by analyzing the spatio-temporal evolution of scattering information obtained from an imaging modality of choice, such as bright-field microscopy [26, 27].

DDM has demonstrated versatility in studying various biological systems, including active transport and advection in *Drosophila* ooplasm [28], microorganism motility [29–31], cytoskeletal dynamics of *in vitro* systems [32, 33], protein size determination [34], and intestinal mucus dynamics [35, 36] (for a review, see [37]). As a microrheological tool, DDM provides direct access to the intermediate scattering function (ISF) of a system, specifically its real part, denoted as $\Re\left[f\left(q,\Delta t\right)\right]$ [26, 27].

* conrad.moeckel@mpzpm.mpg.de
** jochen.guck@mpzpm.mpg.de

The ISF quantifies fluctuations in scatterer positions over time; more technically, it represents the spatial Fourier transform of the particle displacement distribution, known as the van Hove function $G(\Delta r, \Delta t)$ [38]. Within the DDM framework, the ISF is typically expressed in terms of lag time Δt and is derived from differences in a series of digital microscope images $I(\boldsymbol{x}, t)$ in the spatial Fourier domain

$$\begin{aligned} D(q, \Delta t) &\equiv \langle |I(\boldsymbol{q}, t) - I(\boldsymbol{q}, t + \Delta t)|^2 \rangle_{|\boldsymbol{q}|,t} \\ &\equiv A(q) \{1 - \Re [f(q, \Delta t)]\} + B(q), \end{aligned} \tag{1}$$

where $D(q, \Delta t)$ represents the DDM observable, and $\langle \dots \rangle_{|\boldsymbol{q}|,t}$ denotes the time and azimuthal average at the displacement mode $q = |\boldsymbol{q}| = 2\pi/\Delta r$ (see Fig. 1B). The term $A(q) \equiv \hat{A}(q) + B(q)$ is related to the static structure factor via the amplitude best estimate $\hat{A}(q) \simeq S(q)$, and $B(q)$ accounts for the noise characteristics of the camera in use [27] (details in Fig. 1 and Appendix A). The experimentally accessible time and length scales, associated with the lag time Δt and the displacement modes q, respectively, are determined by the frame rate of the camera and the optical magnification of the imaging system employed. The choice of these parameters influences the processes captured by the ISF $\Re [f(q, \Delta t)]$ and the consequent extraction of biologically relevant information, such as protein diffusivities [34].

In this study, we employ bright-field DDM to investigate the collective dynamical properties of high-speed supernatant *Xenopus laevis* egg extract (HSS), which serves as a simplified model system for eukaryotic cytoplasm (Fig. 1A). HSS is a highly dynamic and heterogeneous system, predominantly consisting of a complex mixture of proteins at physiological concentrations [21, 39]. The measured ISF of HSS exhibits characteristics of subdiffusive fractional Brownian motion (fBm) and non-Gaussian tails, phenomena frequently associated with intracellular environments [40–45]. To accurately describe these observations, we propose an empirical model that integrates fBm with an inverse Gaussian distribution of diffusivities, motivated by an underlying size distribution of scatterers within HSS [46]. This model not only provides a robust fit to our experimental data but is also validated by Monte Carlo (MC) simulations.

Furthermore, we study the dynamical behavior of HSS under active (energy addition) and passive (energy depletion) conditions. Our results indicate that HSS maintains stationary behavior, that is, independence of the ISF on the absolute measurement time when ATPase activity is inhibited. Conversely, the addition of ATP and GTP induces non-stationary dynamics, highlighting the influence of energy-driven processes on cytoplasmic behavior.

In addition to the role of cytoplasmic properties, it is well recognized that a significant portion of the mechanical response and behavior of cells arises from cytoskeletal contributions [47]. Characterizing the physical properties of the cytoskeleton is an active field of research in contemporary biophysics. These properties have profound implications for understanding diseases such as cancer, as well as for maintaining tissue homeostasis, morphogenesis, and cell motility [48, 49]. Consequently, it is particularly intriguing to explore the applicability of DDM in inferring cytoskeletal properties within the context of the *Xenopus laevis* egg extract. To study the role of the cytoskeleton in modulating cytoplasmic dynamics, we stabilize microtubules (MTs). We find that stabilizing MTs introduces a secondary characteristic timescale in the ISF. This phenomenon is effectively modeled using a two-state fBm approach, suggesting that the MT network invokes distinct, subdiffusive characteristics indicative of a viscoelastic response. These assumptions are corroborated by MC simulations of a freeze-in scenario, in which the MT network acts as a length scale–dependent thermal sieve.

Remarkably, these three distinct cytoplasmic conditions (macromolecular composition, energy addition, and introduction of a cytoskeleton) result in similar degrees of crowdedness yet distinct diffusivities.

Our findings validate DDM, combined with MC simulations for generating image representations of anomalous statistical processes, as a powerful, label-free technique for quantitatively assessing the subdiffusive and viscoelastic properties of the cytoplasm across relevant time and length scales. With this work, we provide new insights into the active violation of stationarity and the dynamical properties of the cytoskeleton in biologically significant, heterogeneous environments. This study not only advances our understanding of cytoplasmic dynamics but also demonstrates the broader applicability of DDM as a label-free tool for probing complex, heterogeneous biological systems at the subcellular scale.

II. RESULTS

A. The Cytoplasm is Crowded and Heterogeneous — *Redux* —

As outlined in the introduction, previous studies have identified two striking features of the cytoplasm through the analysis of tracer particle trajectories: 1) viscoelastic subdiffusion and 2) non-Gaussian displacement distributions [40–44]. In this section, we introduce these concepts within the framework of DDM and apply them to our measurements of HSS to investigate its dynamical properties in a label-free manner. The theoretical derivations supporting these concepts are provided in Appendix B.

1. *Viscoelastic Subdiffusion*

Viscoelastic subdiffusion is commonly described by fractional Brownian motion (fBm) and phenomenologically arises from the anomalous scaling behavior of the

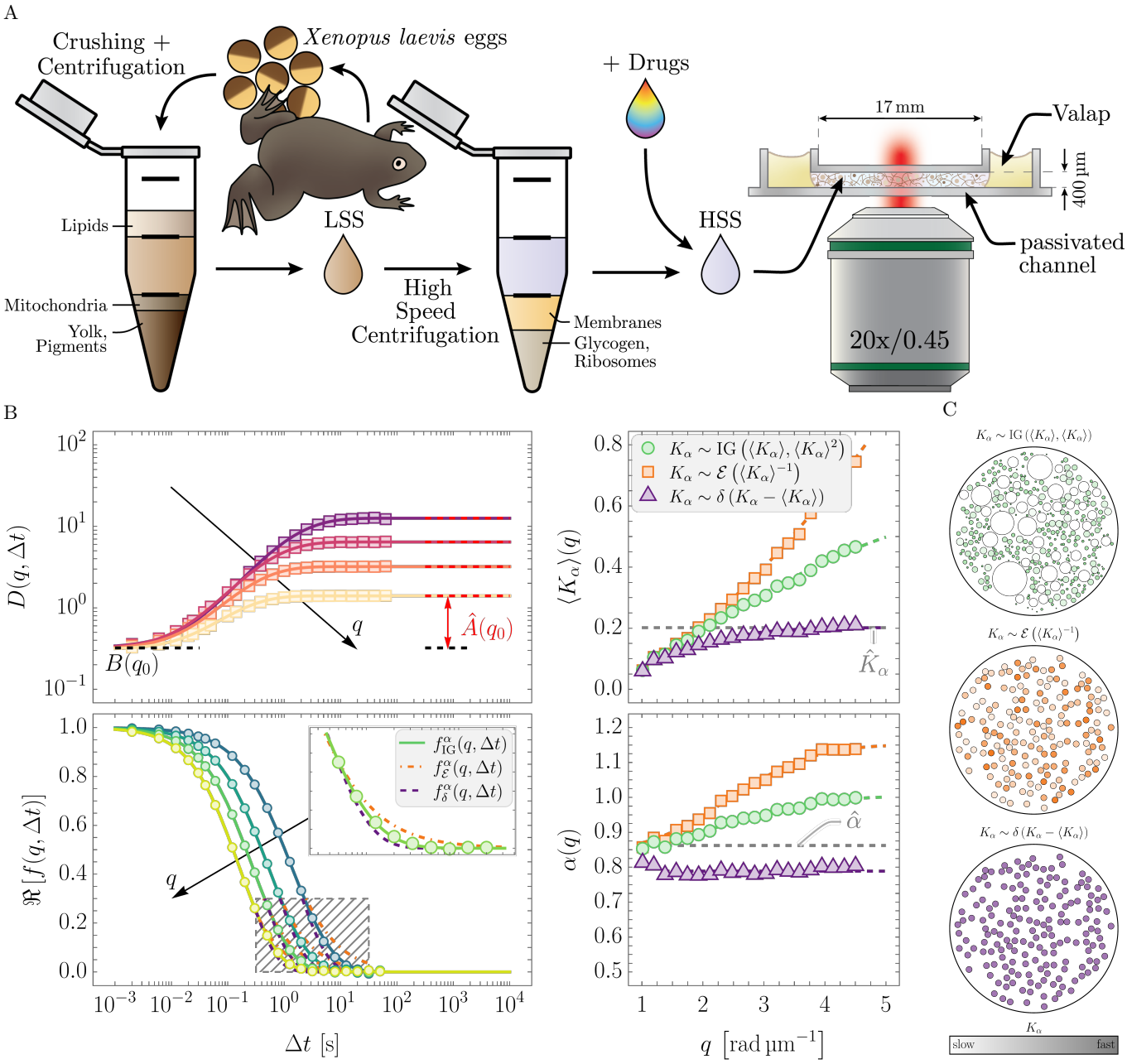

FIG. 1: Schematic overview of the experimental setup and results of this study: A: Production of high-speed supernatant *Xenopus laevis* egg extract (HSS) from low-speed supernatant (LSS) via high-speed centrifugation and loading of the sample into a commercially available microfluidic channel (dimensions not to scale). B: Left: Exemplary azimuthally averaged DDM map $D(q, \Delta t)$ over the lag time Δt (top), where the black arrow indicates the dispersion over the displacement modes q, the black dashed line indicates the camera noise measurement $B(q_0)$, and the red double arrow indicates the amplitude estimate $\hat{A}(q_0)$ (see Section IV H) for an exemplary displacement mode $q_0 \approx 4.13\,\mathrm{rad\,\mu m^{-1}}$ and corresponding real part of the intermediate scattering function $\Re[f(q, \Delta t)]$ (bottom) computed using Eq. (1). The inset shows the best fits of the three different analytical models Eqs. (4) to (6) discussed in the main text (see Appendix B for derivations) to the data for an exemplary displacement mode $q_0 \approx 3.44\,\mathrm{rad\,\mu m^{-1}}$. Right: Extracted best-fitting parameters from the three analytical models as a function of displacement mode q; top: Dimensionally normalized mean fractional diffusivity $\langle K_\alpha \rangle(q)$, and bottom: fractional exponent $\alpha(q)$. The colorful dashed lines are sigmoidal fits, and the gray dashed lines indicate the inferred parameter estimates $\hat{K}_\alpha$ and $\hat{\alpha}$ based on MC simulations (see Fig. B2). C: Representative schematic representations of the underlying assumptions of the analytical models shown in B; top: Scatterers exhibit a size distribution and a distribution of (fractional) diffusivities according to a generalized Stokes–Einstein relation Eq. (B9) with a constant 'fractional' viscosity η_α, middle: All scatterers have the same size but an exponential distribution of (fractional) diffusivities, bottom: All scatterers have the same size and (fractional) diffusivity.

(ensemble and/or time-averaged) mean-squared displacement (MSD) $\langle[\Delta r(\Delta t)]^2\rangle \propto (\Delta t)^\alpha$, with $0 < \alpha < 1$. fBm features stationary increments $\Delta r(\Delta t)$ [50, 51], which posits that the ISF is only dependent on the lag time Δt. In the context of DDM, the corresponding ISF is a Gaussian, given by

$$f^\alpha(q, \Delta t) = \exp\left[-q^2 K_\alpha (\Delta t)^\alpha\right], \tag{2}$$

where K_α is the fractional diffusivity in units of $\mathrm{m}^2\,\mathrm{s}^{-\alpha}$. It is noteworthy that such a fractional time scaling of the displacement distribution can also be formally derived by introducing a power-law memory kernel to the generalized Langevin equation, or by considering fractional Gaussian noise [42, 52–54]. A physical interpretation of the fractional diffusivity is not straightforward because of its fractional dimensionality. Specifically, any two fractional diffusivities with different fractional exponents cannot be directly compared; nevertheless, their magnitudes provide important information. To avoid confusion, we consistently (implicitly or explicitly) refer to dimensionally normalized fractional diffusivities $K_\alpha/\mu\mathrm{m}^2\,\mathrm{s}^{-\alpha}$ throughout this study. The same applies to derived observables. The fractional exponent α may serve as an indicator of 'molecular crowdedness' [9, 55, 56]; specifically, the lower α, the more crowded the system. Mechanistically, subdiffusive fBm resembles a power-law material with viscoelastic properties, elegantly captured by the spring-pot model [57]; $\alpha \to 0$ indicates a more elastic, 'spring-like' response of the system, and $\alpha \to 1$ a more viscous, 'dashpot-like' behavior. Concordant with Eq. (2), for $\alpha = 1$ the system is purely viscous, and the scatterers undergo Brownian motion. We note that for fBm, the fractional exponent α is historically referred to as the Hurst exponent $H \equiv \alpha/2$. However, for the sake of simplicity and clarity of notation, we will use α instead of $2H$ throughout this study.

2. *Non-Gaussian Displacement Distributions and Superstatistics*

The origin of the observed non-Gaussian tails in the van Hove distribution $G(\Delta r, \Delta t)$ is associated with heterogeneity in the system, specifically a distribution of diffusivities $\mathcal{P}(K_\alpha)$ [41]; a concept known as superstatistics [40, 58]. In the context of DDM, this straightforwardly translates to

$$f^\alpha_{\mathcal{P}}(q, \Delta t) = \int \mathrm{d}K_\alpha\, \mathcal{P}(K_\alpha)\, f^\alpha(q, \Delta t). \tag{3}$$

A trivial case occurs when the diffusivity is delta-distributed at a mean value $\langle K_\alpha\rangle$, i.e., $K_\alpha \sim \delta(K_\alpha - \langle K_\alpha\rangle)$, which yields the ISF

$$f^\alpha_\delta(q, \Delta t) = \exp\left[-q^2\langle K_\alpha\rangle(\Delta t)^\alpha\right]. \tag{4}$$

Although this homogeneity assumption fails to account for non-Gaussian tails in the ISF, it serves as a conservative assumption in the following analysis.

Alternatively, an exponential distribution of diffusivities, $K_\alpha \sim \mathcal{E}(\langle K_\alpha\rangle^{-1})$ (Eq. (B1)), as employed in the context of bacterial cytoplasm in the work of [43] and further discussed in [40, 59], leads to

$$f^\alpha_{\mathcal{E}}(q, \Delta t) = \left[1 + q^2\langle K_\alpha\rangle(\Delta t)^\alpha\right]^{-1}. \tag{5}$$

Eq. (5) accounts for a degree of heterogeneity in the microenvironment of scatterers, including the possibility of scatterers being immobile. However, because DDM evaluates changes in intensity over time, very slow or immobilized scatterers contribute only weakly to the signal, potentially rendering Eq. (5) less applicable for DDM experiments. Furthermore, this particular notion of superstatistics is consistent with a homogeneous population of tracer particles, which is not necessarily valid for the scatterers inherent to the HSS. Since DDM is heavily dependent on the (optical) properties of the scatterers, it is expected that the extracted ISF is sensitive to heterogeneities in the scatterer population, such as a size distribution. The notion of a heterogeneous scatterer population in the HSS is well motivated by considering the molecular weight (MW) distribution of proteins comprising the proteome of *Xenopus laevis* [46]. Besides a strong dependence on the charge, [5] found an inverse relationship between the MW and the diffusivity of various proteins in *Xenopus* egg extract, consistent with the Stokes–Einstein relation [60]. This concept may be extended to protein complexes and larger aggregates, which presumably constitute the measured scattering information.

To describe such a heterogeneous scatterer population in the HSS, we propose using an inverse Gaussian (IG) distribution, $K_\alpha \sim \mathrm{IG}(\langle K_\alpha\rangle, \langle K_\alpha\rangle)$ (Eq. (B4)), which does not include $K_\alpha = 0$ (immobile scatterers) in its support. This assumption is motivated by a generalized Stokes–Einstein relation hypothesized as $K_\alpha \propto 1/R$, where R is the scatterer radius. The resulting ISF reads

$$f^\alpha_{\mathrm{IG}}(q, \Delta t) = \exp\left[1 - \sqrt{1 + 2q^2\langle K_\alpha\rangle(\Delta t)^\alpha}\right], \tag{6}$$

which exhibits non-Gaussian tails, although less pronounced than those in Eq. (5) (see Fig. B1). To simplify the model, in concordance to the properties of the exponential distribution, we assumed in Eq. (6) that the mean and standard deviation of the IG distribution are equal. The general form of Eq. (6) is provided in Appendix B, Eq. (B7).

It is important to note that various diffusivity distributions can describe such heterogeneous populations. For instance, [61] previously used a gamma-distributed diffusivity to model the heterogeneous movement of nematodes; we include the corresponding ISF expression in Appendix B, Eq. (B12). While the gamma distribution offers suitable characteristics, its shape and scale parameters are less straightforward to interpret compared to the IG distribution. The outlined approach could also be extended to the generalized gamma distribution (see [62] and references therein).

Adding to this discussion, the dynamics of polydisperse protein-rich clusters in the context of DDM have been studied in [63]. There, the authors expanded the ISF in Eq. (3) for $\alpha = 1$ around the mean diffusivity $K_\alpha - \langle K_\alpha \rangle$ up to second order. Assuming that the first and second moments of the diffusivity distribution exist, this procedure yields the approximate solution of Eq. (3), a non-Gaussian ISF

$$f_2^\alpha(q, \Delta t) = f_\delta^\alpha(q, \Delta t) \left[1 + \frac{\mu_2}{2} q^4 (\Delta t)^{2\alpha}\right], \tag{7}$$

as further detailed in [64]. The 'relative heterogeneity' of the scatterer population $\kappa \equiv \mu_2/\langle K_\alpha \rangle^2$ may be defined, where

$$\mu_2 \equiv \int \mathrm{d}K_\alpha \, \mathcal{P}(K_\alpha) \left(\langle K_\alpha \rangle - K_\alpha\right)^2 \tag{8}$$

is the second moment around the mean of the diffusivity distribution of choice, or may be treated as an open model parameter.

We emphasize that the subsequent procedure is largely unaffected by the choice of either gamma or IG distributions, or moment expansion of Eq. (3). However, to maintain consistency with the other model assumptions–specifically having only two open model parameters, $\langle K_\alpha \rangle$ and α–to describe the inherent size distribution of scatterers, we primarily focus on Eq. (6) in the following analysis.

3. Model Fitting and Parameter Extraction

To assess the above theoretical prerequisites in the context of our model system, we acquired image sequences of the HSS, as described in Section IV F and schematically illustrated in Fig. 1A. This data was subsequently analyzed using the DDM algorithm outlined in Section IV H, yielding the ISF data as a function of the displacement mode q and lag time Δt, as shown in Fig. 1B.

Given that it is initially not clear which of the aforementioned theoretical models most accurately represents the experimental system, we fitted Eqs. (4) to (6) to the ISF data as a function of lag time Δt. Through this fitting process, we estimated the mean fractional diffusivity $\langle K_\alpha \rangle$ and the exponent α as functions of the displacement mode q (right panel of Fig. 1B). Although the IG distribution of diffusivities Eq. (6) provided the best fit based on residual analysis, the fitting parameters for all three models exhibited a strong, sigmoidal-like dependence on q, suggesting a discrepancy between the model 'dispersion relations' and the experimental data. We hypothesize that this discrepancy may arise from multiple scatterers with varying diffusivities, sizes, and complex refractive indices contributing to the signal at each q, which effectively blurs the displacement mode information. Such blurring could be described by a convolution of displacement modes

$$f(q, \Delta t) = \frac{1}{\Omega} \int_0^\infty \mathrm{d}q' \, f(q', \Delta t) \mathcal{K}(q, q'), \tag{9}$$

where $\mathcal{K}(q, q')$ is a (imaging) system-dependent convolution kernel and Ω is a normalization constant. Eq. (9) accounts for the possibility that the measured image intensity $I(\boldsymbol{x}, t)$ and the number density $\rho(\boldsymbol{x}, t)$ are not simply related through a linear convolution (see Appendix A for further information). However, due to our limited knowledge of the sample properties, and thus the absence of a concise (analytical) form for $\mathcal{K}(q, q')$, in the next step, we employed MC simulations to explore the parameter space of a simplified heterogeneous system, and investigate whether this effect can be reproduced using minimal assumptions.

4. Monte Carlo Simulations

The MC simulations described in Section IV G were conducted based on the assumptions outlined above, with the respective parameter configurations listed in Table B1. In brief, trajectories of $N = 2 \times 10^3$ particles, following their respective statistical processes, were generated. The particles were represented as potentially overlapping, opaque disks with a corresponding radius R, plotted on a grid for each time step to emulate the experimental conditions described in Section IV F. Simulated images were analyzed using the DDM algorithm described in Section IV H.

Analyzing the simulated data, we observe that: 1) when simulating fBm processes with a distribution of diffusivities *without* a size distribution of scatterers (Table B1 and Fig. B2A **a)**–**c)**), the input parameters $\langle K_\alpha \rangle$ and α are accurately recovered by fitting the ISF data using the corresponding models; and 2) the general dependence of the fitting parameters on q for these scenarios does not match the experimental observations.

To further investigate this discrepancy, we then performed simulations incorporating both a distribution of diffusivities and a size distribution of scatterers, based on the generalized Stokes–Einstein relation $K_\alpha \propto 1/R$ with a constant 'fractional' viscosity η_α. Specifically, the scatterer radii were assumed to be distributed as $R \sim k_\mathrm{B}\vartheta/(6\pi\eta_\alpha K_\alpha)$ with $K_\alpha \sim \mathrm{IG}(\langle K_\alpha \rangle, \langle K_\alpha \rangle)$, where ϑ denotes the temperature. Although this *ad hoc* assumption is not strictly derived from first principles, it provides a suitable mathematical framework to describe the fBm ISF of a heterogeneous scatterer population in a quasi-homogeneous fluid.

Simulated data under these conditions show qualitative agreement with the experimental fitting parameter dependencies on q for all three theoretical models employed (Appendix B; Table B1 and Fig. B2A**d)**). This indicates that fBm with a distribution of diffusivities stemming from a size distribution of scatterers effectively captures the complexity present in the experimental DDM data. However, we point out that the magnitude of this effect observed in the simulations is lower than for the experiments. This is likely due to additional heterogeneities in the HSS, which are not captured by our simplistic simu-

lations. Due to the absence of a concise analytical solution of Eq. (9), accurately inferring the underlying system parameters from the data remains challenging. Nonetheless, through a heuristic analysis of the simulated data (for a range of reasonable parameter values), we developed a method to accurately estimate the system parameters from the experimental data, which is described in the following.

5. *System Parameter Estimation*

For the fractional exponent α, we used the estimates obtained by fitting the ISF data with Eq. (6) for each q. We then defined $\hat{\alpha} \equiv \alpha_{\mathrm{IG}}(q \to 1\,\mathrm{rad}\,\mu\mathrm{m}^{-1})$ based on the lower limit of the experimentally accessible q values from a sigmoidal fit. As motivated previously, the *dimensionally normalized* best estimate of the fractional diffusivity $\hat{K}_\alpha$ is obtained similarly to the fractional exponent by fitting the ISF with Eq. (4) and taking the upper limit of q from a sigmoidal fit, yielding $0.5\tilde{K}_\alpha \approx \hat{K}_\alpha \equiv \langle K_\alpha^\delta \rangle(q \to \pi/\epsilon)$, which curiously approximates half the median of the inverse Gaussian distribution $\tilde{K}_\alpha$ for the range of simulated scenarios. Here, ϵ is the empirically determined effective pixel size of the experimental setup (see Section IV F for further information). The procedure outlined is illustrated in Fig. 1B (right), and the comparison between simulation inputs and according best estimates is presented in Figs. B2B and B2C.

6. *Experimental Results*

Applying this paradigm to a series of eight consecutive measurements ($N = 3$) depicted in Fig. 2 (HSS control), we observe that HSS exhibits stationary behavior, or more accurately, stationarity of the increments, over the observed time window of approximately 130 min, excluding the initial equilibration phase. This initial equilibration phase is presumably constituted by shear stresses stemming from pipetting and capillary forces employed to float the sample into the microfluidic channel. Excluding the first data point ($t > 18.5$ min), our DDM analysis yields the following long–time-averaged parameter estimates: $\langle \hat{\alpha} \rangle_t = 0.877 \pm 0.021$, and $\langle \hat{K}_\alpha \rangle_t = 0.181 \pm 0.013$, which is in agreement with the notion of cytoplasmic viscoelastic subdiffusion. Additionally, we employed the moment-expanded approximate ISF Eq. (8) to obtain an estimate of the relative heterogeneity of the scatterer population κ without making explicit assumptions about an underlying diffusivity distribution. We observe that $\kappa(q \gtrsim 3.5\,\mathrm{rad}\,\mu\mathrm{m}^{-1}) \approx$ const. (not shown here), and take the median $\pm$ 68% confidence interval (CI) over $3.5\,\mathrm{rad}\,\mu\mathrm{m}^{-1} \leq q \leq \pi/\epsilon$ as our best estimate. As shown in Fig. 2, $\hat{\kappa}(t)$ remains approximately constant up to the initial equilibration phase of the system. The time-averaged best estimate is given by $\langle \hat{\kappa} \rangle_t = 0.255 \pm 0.023$, which is–expectedly–higher than the values reported in [63] for solutions of hemoglobin A and lysozyme.

To further corroborate the concept of cytoplasmic crowdedness in the context of our model system, we analyzed low-speed supernatant *Xenopus laevis* egg extract (LSS) (Fig. 1A). Unlike HSS, LSS contains larger macromolecular components, including membranes, ribosomes, and glycogen [65], which are expected to increase the degree of crowdedness. Accordingly, we hypothesized that LSS would exhibit a smaller fractional exponent $\hat{\alpha}$ than HSS. Repeating the same measurement paradigm as outlined before, we observe that LSS maintains stationary behavior over the measurement time (Fig. 2, LSS control) following an initial equilibration phase. Excluding the first data point, the average parameter best estimates for LSS are $\langle \hat{\alpha} \rangle_t = 0.763 \pm 0.016$, $\langle \hat{K}_\alpha \rangle_t = 0.030 \pm 0.004$, and $\langle \hat{\kappa} \rangle_t = 0.39 \pm 0.06$. We note that our estimates of the fractional exponents for both HSS and LSS are in good agreement with the values reported in [21], using PT and FCS.

These findings indicate a more crowded and heterogeneous environment in LSS compared to HSS, as well as a more elastic response, underscoring the influence of macromolecular composition on cytoplasmic dynamics. Our label-free DDM approach recapitulates that the cytoplasm is crowded and heterogeneous, allowing us to quantify collective differences between HSS and LSS.

B. Actively Broken Stationarity

Stationarity is a fundamental concept in statistical mechanics, which posits that the ISF of a system is dependent on the lag time Δt, but not the absolute measurement time t. This concept constitutes a necessary, yet not sufficient, criterion for ensuring that temporal measurements reliably reflect the ensemble statistical properties of a system. In living biological matter, the assumption of stationarity can break down (either persistently or transiently) owing to the prevalence of non-equilibrium dynamics and intrinsic heterogeneities introduced by active molecular processes [51, 66, 67]. Non-stationarity of a system may be also associated with aging [68].

Previously, we observed that the HSS exhibited stationary behavior within the observation time. To investigate whether stationarity can be actively disrupted and how the system parameters change over time, we introduced ATP and GTP to stimulate energy-dependent processes, such as polymerization and motor protein activity [2] (see Section IV D). We denote this condition as 'active HSS' in the following. As a control, we also considered the case where ATPase activity was depleted by adding Vanadate, which we denote conversely as 'passive HSS' (see Section IV E).

Employing the previously generated insights, we examined the time evolution of the DDM-detectable statistical processes inherent to HSS under these conditions. Anal-

ogously, we performed consecutive DDM measurements over a total duration of approximately 130 min, operating under the assumption that the stationarity-breaking timescale is much slower than a full relaxation of the measured ISF for the accessible displacement modes q. In other words, we assume that the observable system behaves approximately stationary during each individual measurement (110 s), but undergoes significant changes over longer periods ($\propto$ 10 min). The results of these measurements are displayed in Fig. 2. As becomes evident

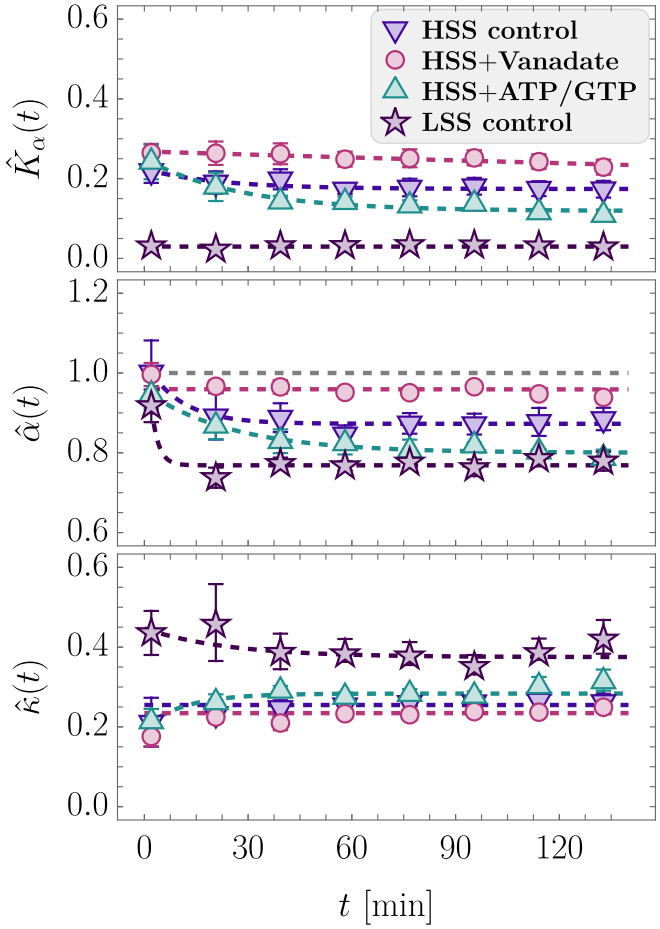

FIG. 2: Results of the fitting procedure for the dimensionally normalized fractional diffusivity $\hat{K}_\alpha(t)$ (top), corresponding fractional exponent $\hat{\alpha}(t)$ (middle), and the relative heterogeneity of the scatterer population $\hat{\kappa}(t)$ (bottom), as described in the main text, for the cases of HSS (control; purple down-triangles), HSS + Vanadate (red circles), HSS + 20x Energy Mix (+ATP/GTP; teal up-triangles), and LSS (control; purple stars) over the experiment time t. Each data point represents the mean ± pooled SEM of three independent measurements (see Section IV I), and the dashed lines represent the respective fits of Eq. (10) to the data.

that while the inferred system parameters of the passive HSS show little to no time dependence, the active HSS exhibits a decrease in both $\hat{K}_\alpha$ and $\hat{\alpha}$ over time, which appears to be less pronounced for long times. Interestingly, the active HSS becomes more subdiffusive than the HSS control, attaining a fractional exponent comparable to that of the LSS (see Table I). In contrast, the passive HSS is consistently less subdiffusive, that is, it exhibits almost Brownian-like diffusion due to the dilution of the HSS upon drug addition, as detailed in Section IV E.

Assuming that the active HSS undergoes a transition from an initial state $\psi_\mathrm{i}(\hat{\alpha}^\mathrm{i}, \hat{K}^\mathrm{i}_\alpha)$ to a final state $\psi_\mathrm{f}(\hat{\alpha}^\mathrm{f}, \hat{K}^\mathrm{f}_\alpha)$ at a certain rate $1/\tau_\psi$, we fitted the time series with a sigmoidal function

$$\psi(t) = (\psi_\mathrm{i} - \psi_\mathrm{f}) \exp\left[-t/\tau_\psi\right] + \psi_\mathrm{f}, \tag{10}$$

to determine the characteristic timescales $\tau_{\hat{K}_\alpha} = (27.57 \pm 6.11)$ min and $\tau_{\hat{\alpha}} = (25.6 \pm 4.8)$ min, which coincide well within the margins of uncertainty. We hypothesize that this active mechanism of increasing the crowdedness of the system to a more viscoelastic response is linked to self-assembly processes and the formation of structures akin to 'protocells', which was previously characterized in LSS [6, 14, 21]. The concordance between the two characteristic timescales indicates that both $\hat{K}_\alpha(t)$ and $\hat{\alpha}(t)$ could be connected to a common underlying non-equilibrium process. We note that this phenomenon could be further interpreted by means of multifractional Brownian motion [69]. Repeating this analysis for the passive HSS, we did not obtain a timescale that is meaningfully different from zero for either quantity within the measurement period, indicating conserved stationarity. A numerical summary of the results is provided in Table I and plotted in Fig. 6.

Examining the relative heterogeneity of the scatterer population over time, $\hat{\kappa}(t)$, we find that the values for the passive HSS remain approximately constant up to the initial equilibration phase. The corresponding time-averaged estimate agrees well with the value obtained for the unperturbed HSS (HSS control; see Table I). In contrast, the active HSS shows a subtle time dependence in $\hat{\kappa}(t)$, and the final value is higher than those of the passive HSS and the control, consistent with the notion of actively induced heterogeneities.

C. Microtubule Networks Mediate Dynamical Hierarchies

In the next phase of our study, we investigated how the presence of a cytoskeletal component, namely microtubules (MTs), alters the dynamic scattering signature of the HSS. Specifically, we stabilized MTs by adding Taxol to the HSS, which induces the formation of a network within the microfluidic channel that undergoes bulk contraction, as depicted in Fig. 5A [70, 71]. Foster *et al.* [70, 71] demonstrated that this contraction phenomenon is significantly correlated with dynein activity and Taxol concentration. While these contractions are noteworthy, they typically occur on a much larger length scale ($\propto$ 1 mm) than our experimental field of

Condition	$\hat{K}_\alpha$	$\hat{\alpha}$	$\hat{\kappa}$
HSS Control	0.181 ± 0.013	0.877 ± 0.021	0.255 ± 0.023
HSS+Vanadate	0.250 ± 0.015	0.955 ± 0.012	0.232 ± 0.017
HSS+ATP/GTP	0.109 ± 0.013	0.787 ± 0.021	$0.314^{+0.030}_{-0.023}$
LSS Control	0.030 ± 0.004	0.763 ± 0.016	0.39 ± 0.05

TABLE I: Numerical results of the DDM analysis of the cytoplasm described in the main text; best estimates of the dimensionally normalized fractional diffusivity $\hat{K}_\alpha$, the fractional exponent $\hat{\alpha}$, and the relative heterogeneity of the scatterer population $\hat{\kappa}$ for different conditions across three independent repetitions, respectively. For the case HSS+ATP/GTP, we report the final value of our time series measurement (see Fig. 2) and for the other cases, we report the long time averages with corresponding uncertainty estimates, excluding the first data point where the system was not well equilibrated (see Section IV I and the main text for further information).

view ($\approx$ 136 µm), and the direction and magnitude of the contractile motion of the MT network are highly dependent on the position within the channel, as seen in Fig. 5A. This spatial variability complicates the extraction of meaningful information using our experimental DDM configuration. To mitigate the effects of contractile motion, we attempted to passivate the HSS by adding Vanadate; however, Vanadate addition did not fully inhibit contraction, consistent with observations in [70] involving additional inhibition of dynein. While the remaining contractile motion could be caused by the cumulative effects of other molecular motors, we found that in our experimental system, contractions were minimized at low Taxol concentrations. Therefore, to reduce contractions within the observation time while maintaining a MT network, we selected a Taxol concentration of $c_{\mathrm{Tax}} = 0.25\,\mu\mathrm{M}$ as optimal for investigating fluctuations associated to the network. We note that this concentration is lower than the concentrations used in [70, 71], which cover $1\,\mu\mathrm{M} \leq c_{\mathrm{Tax}} \leq 25\,\mu\mathrm{M}$. Strikingly, the resulting data presented in Fig. 3 exhibit a second characteristic timescale.

This observation prompts the question: how can this result be interpreted? From a phenomenological perspective, the data are well described by an effective two-state fBm model

$$f_\delta^{\alpha\beta}(q,\Delta t) \equiv \varphi(q) f_\delta^{\alpha}(q,\Delta t) + (1-\varphi(q))\, f_\delta^{\beta}(q,\Delta t), \quad (11)$$

where $\varphi(q)$ represents the length scale–dependent occupation of the respective states (see Fig. 3A). Eq. (11) is governed by the idea of separating the measured ISF into contributions associated with the MT network (β-state; slow timescales) and cytosolic contributions (α-state; fast timescales). Similar models have been employed to describe heterogeneous dynamics in two-dimensional glassy colloids [72], and bidisperse colloidal suspensions [73]. A general theoretical derivation for two-state Markovian switching models was presented in [74]; in our context, Eq. (11) can be interpreted as a 'frozen mixture', where there is no switching between states. Instead, the two states correspond to distinct, non-interchangeable entities. We hypothesize that the β-state could be associated with the dynamic scattering information of either 1) the MT network, 2) larger objects potentially captured by the network, or a combination of both, while the α-state represents information connected to smaller particles [75].

Fitting Eq. (11) to the experimental ISF, as shown in Fig. 3A, and applying suitable constraints, we obtained the five parameters as functions of the displacement mode q. By this analysis, we find that the mean fractional diffusivities $\langle K_\alpha \rangle$ and $\langle K_\beta \rangle$ along with their corresponding fractional exponents α and β exhibit an approximately constant relationship across the range of available q values. Based on this observation, and consistent with the previous analysis, we took half of the median $\pm$ 68% CI for the fractional diffusivities, and the median $\pm$ 68% CI for the fractional exponents over q as our best estimates. Conversely, $\varphi(q)$ displays a sigmoidal dependence on q (see Fig. 3B).

Building on [72], where a similar ISF model was employed, we modeled $\varphi(q)$ using a stretched exponential function

$$\varphi(q) = (\varphi_\infty - \varphi_0)\left(1 - \exp\left[-\left\{\frac{\lambda q}{2\pi}\right\}^{\theta}\right]\right) + \varphi_0. \quad (12)$$

Note that we utilize a stretched exponential with an exponent θ, whereas [72] used $\theta = 2$. Fitting Eq. (12) to our data yielded $\lambda = (2.00 \pm 0.29)\,\mu\mathrm{m}$ and $\theta = 2.26 \pm 0.33$ ($N = 3$); the inferred values of φ_0 and φ_∞ showed significant variability from experiment to experiment (not shown here). In our context, λ can be interpreted as a characteristic displacement length scale above which the measured ISF predominantly corresponds to the fluctuations associated with the MT network (β-state) and below which it corresponds more to the cytosolic component (α-state). Furthermore, we observed that the β-state ($\hat{K}_\beta = 0.68^{+0.18}_{-0.13} \times 10^{-2}$, $\hat{\beta} = 0.53^{+0.07}_{-0.04}$) is more subdiffusive than the α-state ($\hat{K}_\alpha = 0.077^{+0.011}_{-0.007}$, $\hat{\alpha} = 0.774^{+0.026}_{-0.025}$) ($N = 3$). This indicates that the assembly of the MT network creates a second dynamical regime characterized by distinct subdiffusive properties. We note that our estimate of the fractional exponent $\hat{\beta}$ is in good agreement with the fractional exponents of actin-microtubule networks obtained in [33] using tracer-particle-based DDM. To further investigate these findings, specifically to examine the hypotheses stated above, model assumptions, and explore a potential mechanism underlying the observed effects, we conducted MC simulations of a simplistic freeze-in model, as elaborated in Appendix B. This freeze-in model is based on the assumption that larger particles become 'trapped' in the MT network, which then imposes new dynamical properties onto them. In brief, we started with an inverse Gaussian distribution

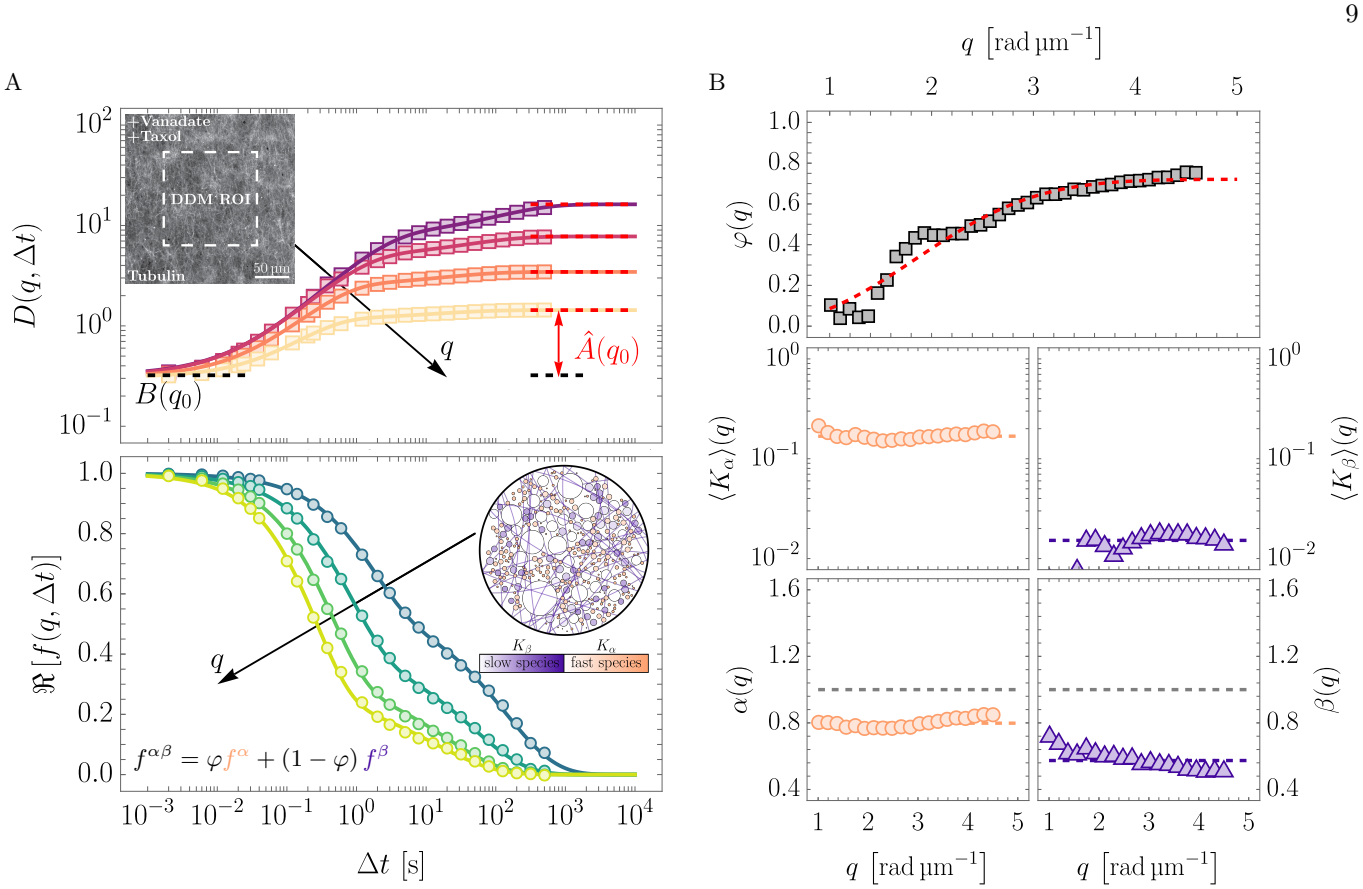

FIG. 3: Results of the DDM analysis of measurements of HSS supplemented with Vanadate (0.5 mM) and Taxol (0.25 µM): A Top: Exemplary azimuthally averaged DDM map $D(q,\Delta t)$ over the lag time Δt (top), where the black arrow indicates the dispersion over the displacement modes q, the black dashed line indicates the camera noise measurement $B(q_0)$, and the red double arrow indicates the amplitude estimate $\hat{A}(q_0)$ (see Section IV H) for an exemplary displacement mode $q_0 \approx 4.13\,\mathrm{rad\,\mu m^{-1}}$. The inset depicts an exemplary fluorescence image of the HyLyte 488-labeled MT network, where the white square indicates the region of interest. A Bottom: Experimental ISF $\Re\,[f\,(q,\Delta t)]$ (circles) and fits of the ISF using Eq. (11) (solid lines). The inset graphic schematically represents the model assumptions, namely a freeze-in/soft caging scenario mediated by the MT network. B: Fitting parameters of the data shown in A as a function of the displacement mode q; top: Mixing parameter $\varphi(q)$ with the red dashed line indicating the best fit to the data using a stretched sigmoidal function (as shown in the inset at the top), middle: Dimensionally normalized fractional mean diffusivities $\langle K_\alpha\rangle(q)$ (orange circles) and $\langle K_\beta\rangle(q)$ (purple up-triangles) with dashed lines indicating the median values, and bottom: Fractional exponents $\alpha(q)$ (orange circles) and $\beta(q)$ (purple up-triangles) with colorful dashed lines indicating the median of the data and gray dashed lines indicating $\alpha = \beta = 1$.

of diffusivities and a corresponding distribution of scatterer radii, as previously described. We then introduced a cutoff probability p such that

$$p = \int_0^{K^*} \mathrm{d}K\, \mathrm{IG}(K; \langle K\rangle, \langle K\rangle), \tag{13}$$

as illustrated in Fig. B3. This cutoff effectively defines two subpopulations of scatterers with distinct size distributions: scatterers with $K \geq K^*$ are assigned to the α-state, and those with $K < K^*$ are assigned to the β-state. The freeze-in mediated by the MT network is then emulated by decreasing the K_β by a certain factor and increasing the crowdedness by decreasing β, while the properties of the α-state remain unaltered. In other words, we interpret the MT network as a thermal sieve that captures larger particles and imposes new dynamical properties on them, while the smaller particles are not affected. This assumption is in line with the observed size-dependent reduction of protein diffusivities in LSS featuring an intact actin network [5], and taking the above characterized viscoelastic effects into account. The results of these simulations are depicted in Fig. B3 and Fig. B4. They demonstrate that our proposed DDM analysis accurately recovers the input parameters within the uncertainty boundaries for a range of different p values. Additionally, we observe the characteristic sigmoidal dependence of $\varphi(q)$, in agreement with the experimental observations. $\lambda(p)$ scales with the cutoff probability p as expected: the lower the value of p, the higher the length scale at which the system behaves more like the β-state

rather than the α-state due to the changes in the size distribution of both populations. Moreover, $\theta(p)$ remains approximately constant across different p values. However, the average value $\bar{\theta}_{\mathrm{Sim}} = 4.7 \pm 0.7$ does not match the experimental observations, likely due to the simplified assumption in the 2D simulation that non-interacting, homogeneous disks sufficiently generate the image displacement distribution comparable to the experimental system. This suggests that the observed secondary time scale in the measured ISF (β-state) can be attributed to the impact of the MT network on the dynamic scattering contributions of the larger particles.

Examining the experimental system over time, as shown in Fig. 4, we observe that the α-state does not show an initial equilibration phase, as apparent in the previous experiments. It exhibits stationary behavior and is consistently more subdiffusive and slower compared to the controls ($\langle \hat{K}_\alpha \rangle_t = 0.276 \pm 0.013$, $\langle \hat{\alpha} \rangle_t = 0.951 \pm 0.013$) ($N = 3$), indicating that the presence of the MT network increases the cytosolic crowdedness, refining the initial model assumptions. The value of $\hat{\beta}$ does not show a significant change over time, up to the last time point, which might indicate the onset of the contraction of the MT network due to residual motor activity, as alluded to earlier. Further, $\hat{K}_\beta$ decreases significantly over time, indicating aging. The origin of this aging effect remains speculative but might be linked to the formation of longer and more stable MT assemblies. Furthermore, both λ and θ do not exhibit meaningful changes over time, although they show large uncertainties, which can be attributed to the fitting approach.

In addition to the above analyses, it is important to note that when we allowed the MT network to contract by adding ATP and GTP to the system, and chose a higher Taxol concentration ($c_{\mathrm{Tax}} = 5\,\mu\mathrm{M}$) to amplify the effect, measurements outside the MT contraction band did not exhibit a double decay in the ISF, as shown in Fig. 5. This observation confirms that the previously quantified secondary anomalous characteristics of the system are indeed attributable to the presence of the MT network and reinforces its specific role in mediating dynamical hierarchies within the cytoplasm.

III. DISCUSSION AND OUTLOOK

In this study, we utilized DDM to explore the dynamic properties of *Xenopus laevis* egg extract, a model system for eukaryotic cytoplasm. Our label-free approach successfully quantified the viscoelastic and heterogeneous nature of the cytoplasm, offering holistic insights into its complex dynamics. Measuring the dynamic properties of HSS with DDM presented significant challenges due to the inherent crowdedness and heterogeneity of the cytoplasmic environment. These challenges were overcome by our phenomenological framework, enabling us to effectively characterize the inherent dynamics.

Initially, we recapitulated that the cytoplasm is both crowded and heterogeneous. The observed features, consistent with viscoelastic subdiffusion and non-Gaussian displacement distributions, suggest that DDM is a useful tool to quantify complex macromolecular interactions and structural heterogeneities. Through MC simulations, we qualitatively connected this heterogeneity to a size distribution of scatterers, effectively described by an IG distribution of diffusivities coupled with a generalized Stokes–Einstein relation. While simulation approaches incorporating specific properties of all macromolecules present in the HSS, such as refractive index (RI), RI increment, mass density, partial specific volume, and charge distributions, would provide valuable insights, they remain computationally prohibitive at present. Nonetheless, the successful application of our more simplistic MC simulations allowed us to approximate and extract relevant system parameters, facilitating a deeper understanding of HSS in the context of DDM.

Further analysis revealed that the HSS exhibited stationary behavior within a long observation time frame ($\approx 130\,\mathrm{min}$). However, introducing ATP and GTP to stimulate energy-dependent processes resulted in non-stationary dynamics, with the system becoming more subdiffusive over time, shifting towards a more elastic response. We further observed that the relative heterogeneity of the scatterer population $\hat{\kappa}$ slightly increased over time. In contrast, passivating the system by depleting ATPase activity with Vanadate maintained stationary behavior, and a similar value of $\hat{\kappa}$ compared to the unperturbed HSS. This distinction underscores the central role of active molecular processes in influencing the observed dynamics of the cytoplasm. Collectively, these findings demonstrate that actively driven processes can lead to a pronounced breakdown of stationarity in HSS, as reflected in the time evolution of key dynamical parameters extracted from ISF analysis. While non-stationarity and related aging phenomena have been discussed in the context of complex systems [51, 68], to the best of our knowledge, there have been no prior experimental studies that combine biochemical perturbations with time-resolved, label-free quantitative ISF analysis in *Xenopus laevis* egg extract. In line with the discussion of [21] (their Fig. 6a), we interpret these findings as an active mechanism that drives the HSS toward sufficient crowdedness and associated (macro)molecular concentrations [76], potentially facilitating subsequent essential biochemical reactions [4]. This mechanism should not be viewed in opposition to the metabolically induced 'fluidization' of the cytoplasm (see e.g., [3, 77]), as both operate at distinct states of the cytoplasm.

Investigating the influence of the cytoskeleton on cytoplasmic dynamics, we stabilized microtubules (MTs) using Taxol and simultaneously passivated the system with Vanadate. This manipulation introduced a distinct second timescale in the intermediate scattering function (ISF), indicative of dynamics associated to the presence of the MT network. The experimental data were effectively described by a two-state fractional Brownian

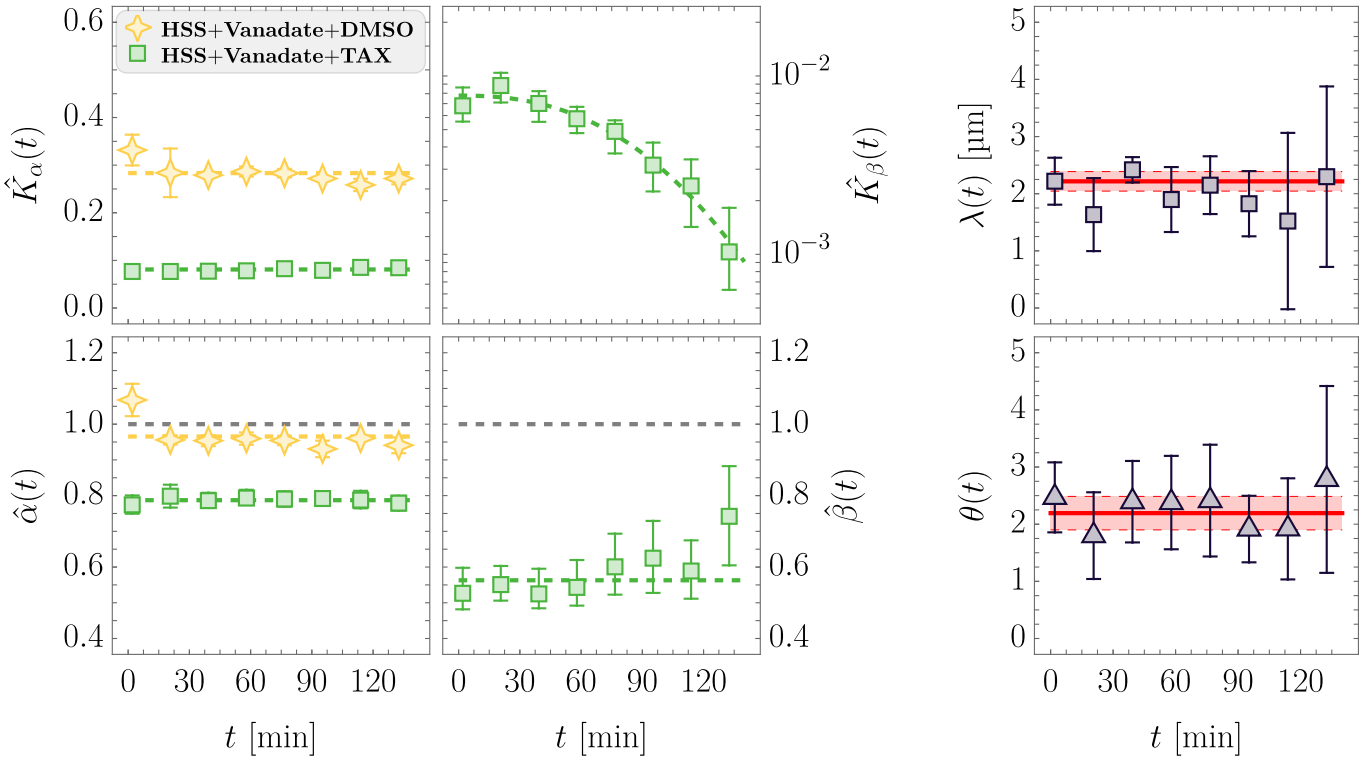

FIG. 4: Results of the DDM analysis of time-series measurements of HSS supplemented with Vanadate (0.5 mM) and Taxol (0.25 µM): Left: Dimensionally normalized fractional diffusivity best estimates $\hat{K}_\alpha$ and $\hat{K}_\beta$ (top row), and fractional exponent estimates $\hat{\alpha}$ and $\hat{\beta}$ (bottom row) for the cases of HSS+Vanadate+Taxol (green squares), and the control HSS+Vanadate+DMSO (yellow stars) as a function of the measurement time t. The colorful dashed lines indicate best fit estimates to the data as shown in Fig. 2, and the gray dashed lines for the fractional exponents indicate $\alpha = \beta = 1$. Right: Fitting results of $\varphi(q)$ with Eq. (12) as a function of the measurement time t; characteristic length scale λ (top) and scaling exponent θ (bottom), where the red lines indicate constant best fit estimates with 68% CIs. Each data point represents the mean ± pooled SEM of three independent measurements (see Section IV I).

motion (fBm) model, allowing us to differentiate between two distinct modes of viscoelastic subdiffusion: a fast subdiffusive α-state and a slower, more subdiffusive β-state. Specifically, we identified that observed image displacements larger than (2.00 ± 0.29) µm are predominantly associated with the β-state, while smaller displacements correlate with the α-state. We further observed that the α-state exhibited slower and more crowded characteristics than the controls, suggesting that the introduction of the MT network not only creates a more elastic response, as reflected by the more pronounced subdiffusive characteristics of the β-state, but also impacts the cytosolic mode of diffusion.

To further substantiate our findings, we conducted MC simulations based on a simplistic freeze-in model. Starting with an IG distribution of diffusivities and an associated distribution of scatterer radii, we introduced a cutoff probability to define two subpopulations of scatterers corresponding to the cytosolic and MT network states, without explicitly simulating the MT network itself. By adjusting the diffusivity of the β-species, the simulations qualitatively replicated the experimental observations, including the sigmoidal dependence of the mixing parameter $\varphi(q)$. While the scaling exponent θ in the stretched exponential fit did not match experimental values. This is likely due to the simplified assumption of using homogeneous disks as scatterers in the simulations, and lead to conclusion that the dynamic scattering information of larger, captured objects contribute to the phenomenological β-state. The overall agreement and accurate recovery of simulation input parameters support the validity and applicability of the two-state fBm model. However, we point out that the proposed mechanism is not sufficient to explain a reduction in $\hat{\alpha}$ or $\hat{K}_\alpha$ of the cytosolic α-state as apparent in the experiments.

Observing the system over time revealed that the cytosolic α-state remained stationary and exhibited consistent subdiffusive behavior. In contrast, the MT network β-state demonstrated signs of aging, characterized by a significant decrease in fractional diffusivity $\hat{K}_\beta$ over time. The underlying mechanisms driving this aging effect remain rather speculative at present, but might be associated to residual motor activity.

To place the main findings of this study in a broader

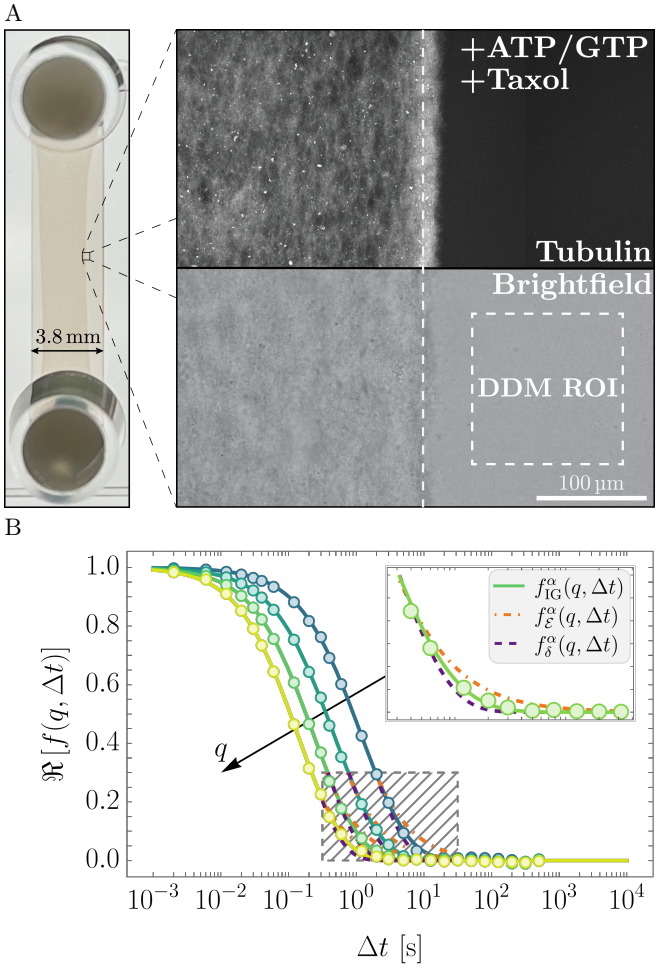

FIG. 5: Results of DDM analysis of HSS with the addition of 20x Energy Mix and Taxol (5 µM): A: Top-view image of the mounting channel approximately 2.5 h after preparation with a clearly visible MT contraction band (left) and corresponding confocal fluorescent (HyLyte 488-labeled tubulin) and bright-field microscopy images of the region indicated by the black square (right). B: Real part of the ISF $\Re[f(q,\Delta t)]$ as a function of the lag time Δt and displacement modes q, obtained with DDM of the region of interest indicated by the dashed white square in A (right).

context, Fig. 6 presents an overview of the explored parameter space, specifically our best estimates of the fractional diffusivity $\hat{K}_\alpha$ and the fractional exponent $\hat{\alpha}$ across all experimental paradigms; notably, we observe that the three distinct experimental conditions investigated in this study: 1) changing the molecular composition (HSS to LSS), 2) addition of energy, and 3) stabilization of a cytoskeletal component (MT network) result in remarkably similar fractional exponents $\hat{\alpha}$, yet different diffusivities $\hat{K}_\alpha$. This intriguing observation necessitates further investigation to determine whether such effects are universally applicable across varying cytoplasmic conditions and potentially across different cell types.

We note that our results are generally in good agreement with the findings of [21, 75, 78], which employed PT and FCS in *Xenopus laevis* egg extracts. This alignment suggests that the diverse numerical methods utilized in this study accurately reflect the system parameters. However, it is important to mention that in [78], the displacement distribution of a homogeneous population of 20 nm probes in *Xenopus laevis* egg extracts was found to be Gaussian, indicating that the observed non-Gaussianity in our DDM measurements indeed arises from a heterogeneous population of scatterers. Furthermore, to our knowledge, a second characteristic subdiffusive timescale mediated by Taxol-stabilized MT networks has not been previously observed in *Xenopus laevis* egg extracts.

Looking ahead, applying our DDM-based findings to living cells, following the works of [28], presents a promising avenue for further research. Investigating further potential parameter-space constraints through osmotic shock experiments [79], studies on senescent cells [48], or disease models [80] could provide deeper insights into cytoplasmic dynamics across diverse biological contexts. Additionally, exploring out-of-equilibrium properties of living matter using concepts such as mean-back relaxation [81, 82] computed from intensity fluctuations could enhance our understanding of active processes within the cytoplasm. Integrating physics-informed artificial intelligence (AI) methods [83] may also prove beneficial in rapidly screening data and inferring complex diffusion behaviors with high spatial resolution.

Finally, advancing simulation techniques to incorporate more realistic representations of cytoplasmic scatterers, including variations in refractive index, aggregation states, and interaction rates (etc.), would enable more precise modeling and interpretation of DDM data. Such improvements could overcome current limitations and facilitate a more comprehensive understanding of the intricate dynamics governing the cytoplasm. Despite the challenges, our study reveals important insights into the subdiffusive, viscoelastic properties of the cytoplasm, demonstrating a promising approach to explore these characteristics at relevant time and length scales in a label-free manner.

IV. MATERIALS AND METHODS

A. High-Speed Supernatant *Xenopus laevis* Egg Extract Production

Low speed supernatant (LSS) and high speed supernatant (HSS) extracts were prepared as described previously [84, 85]. Briefly, freshly laid *Xenopus laevis* eggs were collected and washed with physiological buffers. The first crushing spin was conducted at 19 000 g for 20 min at 4°C, which fractionated the egg into multiple layers. The crude cytoplasmic layer (LSS) was col-

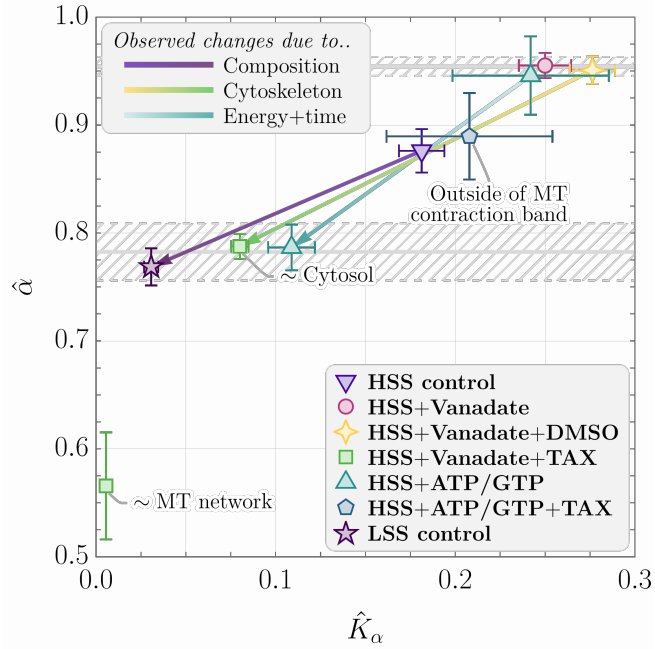

FIG. 6: Overview of the parameter space (best estimates of the dimensionally normalized fractional diffusivity $\hat{K}_\alpha$ and fractional exponent $\hat{\alpha}$) of *Xenopus laevis* egg extract explored in this study. All experiments except HSS+ATP/GTP represent the long time averages with corresponding uncertainty estimates, excluding the first data point where the system was not well equilibrated (see Section IV I and the main text for further information). For the HSS+ATP/GTP condition, we depict the initial and final values from the time-series measurements (symbols), and the arrow indicates the temporal progression. The gray hatched areas and lines represent constant fit estimates of $\hat{\alpha}$ including the cases HSS+ATP/GTP, HSS+Vanadate, HSS+Vanadate+DMSO (top), and HSS+ATP/GTP, LSS control, HSS+Vanadate+Taxol (bottom), respectively, with their 68% CIs. Additionally, for the HSS+ATP/GTP+Taxol condition, data were acquired outside of the contracting MT band (see Fig. 5).

lected and driven into interphase using calcium chloride (final concentration: 0.6 mM). Cycloheximide (final concentration: 0.1 mg ml^{-1}) was added to arrest the eggs in interphase, and cytochalasin D (final concentration: 0.01 mg ml^{-1}) was added to prevent any actin polymerization. The crude LSS was centrifuged again at 260 000 g for 90 min at 4°C. This second spin separated dense components such as membranes, glycogen, ribosomes, and mitochondria from the LSS. The cytosolic layer (HSS) was carefully collected and spun again at 260 000 g for 30 min at 4°C. Aliquots of the final HSS extract were then snap frozen in liquid nitrogen and stored at −70°C.

B. CSF-XB Buffer

CSF-XB buffer was prepared by combining 10 mM HEPES, 50 mM sucrose, 100 mM KCl, 1 mM $MgCl_2$, 0.1 mM $CaCl_2$ (from XB-salt solution), and 5 mM EGTA. The pH was adjusted to 7.7 using KOH. The mixture was stirred continuously, filtered through a 200 nm filter, aliquoted, and stored at 4°C.

C. 20x XB-Salt Solution

A concentrated 20x XB-salt solution was prepared by combining 2 mol l^{-1} KCl, 20 mM $MgCl_2$, and 2 mM $CaCl_2$. The solution was stirred continuously, filtered through a 200 nm filter, aliquoted, and stored at 4°C.

D. 20x Energy Mix

The 20x Energy Mix was formulated by combining 100 mM creatine phosphate, 0.5 mg l^{-1} creatine kinase, 5 mM ATP, and 5 mM GTP. Specifically, 131.6 µg of ATP and 100 µg of GTP were dissolved in 1 ml of double-distilled water and mixed with 571.4 µg of creatine phosphate in 1 ml double-distilled water. Subsequently, 5 µl of a 0.5 mg l^{-1} creatine kinase stock solution was diluted with 95 µl of double-distilled water and added to the mixture. Finally, 3.1 µl of 1 mol l^{-1} $MgCl_2$ stock solution and 2 µl of 1.5 mol l^{-1} DTT were incorporated. The final solution was aliquoted and stored at −70°C.

E. Sample Preparation and Mounting

HSS or LSS aliquots (30 µl) were thawed, briefly centrifuged, and placed on ice to prevent potential microtubule (MT) formation. Drug aliquots (in CSF-XB buffer or DMSO) were kept on ice, and appropriate amounts were added to the HSS. For experiments without MT stabilization, 3 µl of 5.5 mM Vanadate (Sigma S6508) in CSF-XB buffer or 3 µl of the 20x Energy Mix were added, respectively. For experiments involving MT stabilization, 1.5 µl of 11 mM Vanadate in CSF-XB buffer, and consecutively 1.5 µl of 5.5 µM Taxol (Sigma 33069-62-4) in DMSO (Sigma 5.89569) were added. The MT staining was conducted by addition of HyLyte 488-labeled tubulin (Cytoskeleton, Inc. TL670M-A) to 11 mM Vanadate in CSF-XB buffer or 20x Energy Mix, as detailed in the datasheet. The respective sample was then gently pipetted up and down and loaded into a commercially available microfluidic channel (Ibidi µ-Slide VI 0.4). Both the inlet and outlet of the channel were quickly sealed with lukewarm VALAP (1:1:1 vaseline:lanolin:paraffin) to prevent evaporation druring the measurements. The slide was then transferred to the microscope, and measurements were initiated within approximately two minutes.

F. Experimental Setup and Measurement Scheme

Measurements were conducted using an inverted bright-field microscope (Zeiss Axio Observer 3) equipped with a quasi-monochromatic LED (Luminus CBT-120, (623±19) nm) as the light source and a 20x/0.45 objective lens (Zeiss N-Achroplan). 8-bit images (200 px × 200 px) were captured using a CMOS camera (Mikrotron EoSens) with an exposure time of 2 ms. The objective lens was focused near the lower surface of the imaging chamber to minimize axial diffusion effects. Custom `Python` scripts utilizing the open-source `pylablib` library [86] were employed to control the camera. To balance statistical significance and computational efficiency, image acquisition was performed in three phases: 5000 images at 500 Hz, followed by 5000 images at 50 Hz, and finally 5000 images at 5 Hz. The data were stored in an `hdf5` file, along with the relevant metadata.

The effective pixel size was estimated to be $\epsilon = 0.68\,\mu\mathrm{m}\,\mathrm{px}^{-1}$ using a USAF resolution test target (Thorlabs). Displacement modes were calculated as $q = \{2\pi/(h\epsilon), \ldots, \pi/\epsilon\} \approx \{0.0459, \ldots, 4.5945\}\,\mathrm{rad}\,\mu\mathrm{m}^{-1}$, where $h = 200\,\mathrm{px}$ is the image size. Notably, displacement modes $q < 1\,\mathrm{rad}\,\mu\mathrm{m}^{-1}$ were excluded from the analysis due to parasitic contributions, such as mechanical vibrations of the microscope, lower statistics, and incomplete ISF relaxation. Consequently, the presented analysis focused on the range $1 \leq q \leq \pi/\epsilon$.

Fluorescence data were acquired using a Zeiss LSM 980 featuring AiryScan 2.

All samples were measured at a tightly maintained temperature of $\vartheta = (21 \pm 1)°\mathrm{C}$.

G. Simulation Scheme

Simulations of statistical processes were performed using custom `Mathematica` scripts. For a given statistical process, the 2D trajectories of $N = 2\times10^3$ particles $\boldsymbol{s}_j(t)$ with random initial positions and periodic boundary conditions were computed using a Monte Carlo approach, employing `RandomFunction` for the respective statistical process under study. The sample intensity was plotted on a 200 px × 200 px grid as $I_{\mathrm{obj}}(\boldsymbol{x}, t) = \langle I_0 \rangle T(\boldsymbol{x}, t)$, where $\langle I_0 \rangle$ is the background intensity and $T(\boldsymbol{x}, t)$ denotes the transmittance of the sample in focus. The bright-field image generation of a 3D distribution of point-like scatterers has been extensively discussed in, e.g., [87]. For the sake of simplicity, and for reasons outlined in Appendix A 2, we assume here that it is sufficient to map the dynamical complexity of the HSS to disks, i.e., perfectly focused spatially extended spherical particles, with the time-dependent opacity profile

$$o_j(\boldsymbol{x}, t) = \begin{cases} o_0 & |\boldsymbol{x} - \boldsymbol{s}_j(t)| \leq R_j^2 \\ 0 & \text{else} \end{cases}, \tag{14}$$

where $0 \leq o_0 \leq 1$ is the opacity of a particle and $\boldsymbol{s}_j(t)$ is the center of mass of particle j, following the respective trajectory. In this simulation paradigm, we allow the particles to overlap. The radii R_j were computed according to a generalized Stokes–Einstein relation $R_j = k_{\mathrm{B}}\vartheta/(6\pi\eta_\alpha K_\alpha^j)\,\mu\mathrm{m}$, where k_{B} is the Boltzmann constant, ϑ is the temperature of the system, K_α is the (fractional) diffusivity, sampled from a probability density function $\mathcal{P}(K_\alpha)$ (see Appendix A), and η_α is the corresponding 'fractional' viscosity in units of $\mathrm{mPa\,s}^\alpha$. The transmittance of the sample was generated using the `Opacity` option of a `Graphics` object in `Mathematica`, which operates as follows [88]. As an example, for three overlapping particles, the combined opacity follows

$$\begin{aligned} \tilde{o}_{123}(\boldsymbol{x}, t) &= o_1(\boldsymbol{x}, t) + [1 - o_1(\boldsymbol{x}, t)]\,\tilde{o}_{23}(\boldsymbol{x}, t), \\ \tilde{o}_{23}(\boldsymbol{x}, t) &= o_2(\boldsymbol{x}, t) + [1 - o_2(\boldsymbol{x}, t)]\,o_3(\boldsymbol{x}, t), \end{aligned} \tag{15}$$

with $\tilde{o}_{23}(\boldsymbol{x}, t) = \tilde{o}_{32}(\boldsymbol{x}, t)$, i.e., the combined opacity is invariant under permutations in the indices. For N particles, we have accordingly $\tilde{o}_{1\ldots N}(\boldsymbol{x}, t) = o_1(\boldsymbol{x}, t) + [1 - o_1(\boldsymbol{x}, t)]\,\tilde{o}_{2\ldots N}(\boldsymbol{x}, t)$, and so on. Finally, the transmittance is given by $T(\boldsymbol{x}, t) = 1 - \tilde{o}_{1\ldots N}(\boldsymbol{x}, t)$ and the image intensity reads

$$I(\boldsymbol{x}, t) = {}_0\lfloor I_{\mathrm{obj}}(\boldsymbol{x}, t) + \xi(\boldsymbol{x}, t) \rceil^{255}, \tag{16}$$

where ${}_a\lfloor \ldots \rceil^b$ indicates rounding to the nearest integer with lower and upper clipping limits a and b, respectively, emulating an 8-bit image featuring delta-correlated Poissonian noise $\langle \xi(t)\xi(t + \Delta t) \rangle = \mu_0^2 \delta(\Delta t)$, with mean value μ_0, resembling the experimental conditions approximately. In this way, sequences of 1000 images at different frame rates were generated per simulation.

H. Differential Dynamic Microscopy

Differential dynamic microscopy (DDM) analysis was performed using custom `Mathematica` scripts, following standard procedures as described in [27] and outlined in the main text. Briefly, the acquired images were first multiplied by a Blackman-Harris window function to minimize edge effects [89]. Image differences were then computed for various lag times and averaged according to equation Eq. (1). The respective discrete spatial Fourier transforms were calculated and subsequently azimuthally averaged using the `ImageTransform` function in `Mathematica`. The resulting data was then coherently stitched together for each experimental frame rate, taking the element-wise average over the lag-time overlap. Because of concerns about the signal-to-noise ratio and the stationary property of the system under study, this lag-time overlap was consistently chosen to be minimal. For experiments without MT stabilization, we utilized only the data acquired at 500 Hz and 50 Hz to prevent impairing the fitting algorithm by the inclusion of excessive data where the ISF has already fully relaxed, i.e., attaining a value of zero, and to address concerns about

potential non-stationarity of the system at longer time scales. Conversely, for experiments with MT stabilization, we incorporated the data acquired at 5 Hz, as the ISF showed full relaxation only at significantly larger lag times.

The background term $B(q)$ was estimated based on no-sample background measurements at different mean intensities $\langle I_0 \rangle$. A background DDM map $D_0(\langle I_0 \rangle, q, \Delta t)$ was constructed and interpolated over $\langle I_0 \rangle$ (see Fig. 7). For our setup, the background DDM map exhibited close-to-ideal delta-correlated Gaussian noise behavior. Therefore, we averaged over the lag time to obtain a less noisy estimate. By comparing with the intensity of a measurement $\langle I \rangle$, the respective background term was obtained by $B(q) = \langle D_0 (\langle I \rangle, q, \Delta t) \rangle_{\Delta t}$. We adjusted the mean intensity of each measurement to $\langle I \rangle \approx 139$ to fall within an optimal response region of the sensor where the noise level is largely independent of intensity fluctuations, as shown in Fig. 7.

The amplitude term $\hat{A}(q)$ was estimated by fitting either a sigmoidal or double sigmoidal function of the form $\hat{A}(q) + [B(q) - \hat{A}(q)]g(q, \Delta t)$ to the DDM map $D(q, \Delta t)$. Here, $g(q, \Delta t)$ was chosen to be a (double) exponential decay function (see Fig. 1B), and initial points of the amplitude were set as $\hat{A}_0(q) = 2\langle |I(q,t)|^2 \rangle_t$ to improve the fitting procedure. While other amplitude estimation methods exist in the literature, we found this approach to provide the most consistent results, also when applied to simulated data.

Finally, the intermediate scattering function (ISF) was computed by numerically solving equation Eq. (1), and a theoretical model of choice was then fitted to the data to extract the relevant parameters. The goodness of fit was evaluated based on the fitting residuals across both lag times and displacement modes (not shown here).

I. Statistical Analysis

All statistical analyses were performed using custom `Mathematica` scripts. Data fitting and extraction of the best fit estimates of a parameter p along with the corresponding confidence interval (CI) estimates were achieved using the `NonlinearModelFit` function. The pooled SEM, associated with the mean over N experimental repetitions $\overline{p}$, was computed as

$$\hat{\sigma}_{\overline{p}} = \frac{1}{\sqrt{N}} \sqrt{\sigma_p^2 + \overline{\sigma}_{\mathrm{CI}}^2}, \tag{17}$$

where σ_p is the standard deviation of p, and $\overline{\sigma}_{\mathrm{CI}}$ indicates the average of the estimated CIs. The uncertainty estimates for time averages were calculated as

$$\hat{\Sigma}_{\langle \overline{p} \rangle_t} = \sqrt{\langle \hat{\sigma}_{\overline{p}} \rangle_t^2 + \sigma_{\overline{p}}^2}, \tag{18}$$

with the time-averaged pooled SEM $\langle \hat{\sigma}_{\overline{p}} \rangle_t$ and the temporal standard deviation of $\overline{p}$, $\sigma_{\overline{p}}^2$, over N_t time points.

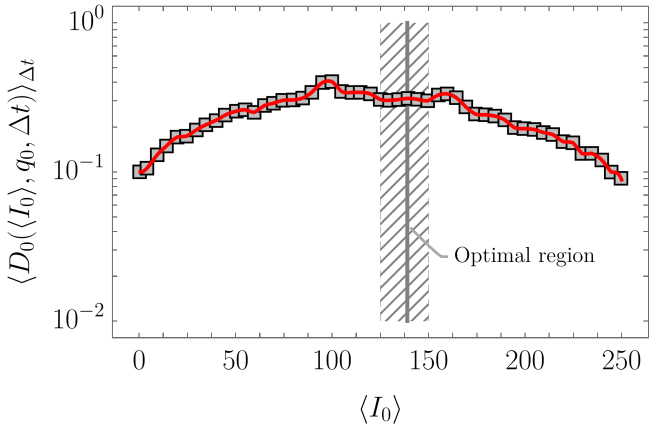

FIG. 7: Noise characteristics of the Mikrotron EoSens CMOS sensor used in this study. The plot shows the average background DDM map $\langle D_0(\langle I_0 \rangle, q_0, \Delta t) \rangle_{\Delta t}$ for a specific displacement mode $q_0 \approx 4.13\,\mathrm{rad\,\mu m^{-1}}$ at various mean intensities $\langle I_0 \rangle$ (black squares) alongside the corresponding interpolation function (red curve). The gray hatched area delineates the optimal mean intensity range for measurements ($125 \leq \langle I \rangle \leq 150$), and the solid gray line indicates the optimized for mean intensity used in this study.

AUTHOR CONTRIBUTIONS

J.G., C.M., and V.Z. conceptualized the project. C.M. developed the methodology, and conducted the experiments. All authors interpreted the experimental results. C.M., and V.Z. conducted the theoretical considerations. All authors interpreted the theoretical results. C.M. wrote the original draft of this manuscript. All authors edited and improved the manuscript. A.B., and S.R. provided the *Xenopus laevis* egg extract. J.G., and V.Z. supervised the project.

DECLARATION OF INTEREST

The authors declare no competing interests.

DATA AVAILABILITY STATEMENT

The data and code that support the findings of this study are available under the following link `link-to-repository`.

ACKNOWLEDGMENTS

The authors thank Manuela Hauke for the preparation of buffers, and Olga Lyraki, Jana Bachir-Salvador,

Tomohisa Toda, Kyoohyun Kim, Shada Abuhattum, Timon Beck, and Sara Kaliman for discussions. Finally, the authors gratefully acknowledge the funding from the Max Planck Society to S.R. and J.G..

Appendix A: Derivations for DDM

In the following, we recapitulate how the DDM observable $D(q, \Delta t)$ is connected to the normalized intermediate scattering function (ISF).

1. The Intermediate Scattering Function

Following the derivations in [90, 91], here we consider the dynamical properties in space and time of a given sample via the number density $\rho(\boldsymbol{x}, t)$, where $\boldsymbol{x} = (x, y)^{\mathrm{T}}$ denotes the 2D Cartesian coordinates in the lateral plane. Assuming that the sample consists of N discrete scatterers, the number, or one-point density and associated density modes are given by

$$\begin{aligned} \rho(\boldsymbol{x}, t) &\equiv \sum_{j=1}^{N} \langle \delta\left[\boldsymbol{x} - \boldsymbol{s}_j(t)\right]\rangle\,, \text{ and} \\ \rho(\boldsymbol{k}, t) &= \sum_{j=1}^{N} \langle \exp\left[-i\boldsymbol{k}\cdot\boldsymbol{s}_j(t)\right]\rangle\,, \end{aligned} \tag{A1}$$

respectively, with $\boldsymbol{s}_j(t)$ being the position of particle j at time t, and $\langle \dots \rangle$ denoting the ensemble average. Further assuming that the N scatterers undergo processes with stationary increments, we introduce the time-averaged, lag-time–dependent van Hove correlation function, or normalized two-point density, as

$$\begin{aligned} G(\Delta\boldsymbol{r}, \Delta t) &\equiv N^{-1} \sum_{i=1}^{N}\sum_{j=1}^{N} \langle \delta\left[\Delta\boldsymbol{r} - \boldsymbol{s}_i(t+\Delta t) + \boldsymbol{s}_j(t)\right]\rangle_t \\ &\equiv G_{\mathrm{s}}(\Delta\boldsymbol{r}, \Delta t) + G_{\mathrm{d}}(\Delta\boldsymbol{r}, \Delta t), \end{aligned} \tag{A2}$$

where $\langle \dots \rangle_t$ denotes time and ensemble averaging in this instance. $G_{\mathrm{s}}(\Delta\boldsymbol{r}, \Delta t)$ is the so-called self-part, the probability density function of the displacements of particle i at time $t + \Delta t$ with respect to itself at time t, and $G_{\mathrm{d}}(\Delta\boldsymbol{r}, \Delta t)$ is the distinct part, the probability density function of displacements of particle $j \neq i$ at time $t + \Delta t$ with respect to particle i at time t. The spatial Fourier transform of the van Hove correlation function is called the intermediate scattering function (ISF), and can be expressed as

$$F(\boldsymbol{q}, \Delta t) \equiv N^{-1} \langle \rho(-\boldsymbol{q}, t)\rho(\boldsymbol{q}, t+\Delta t)\rangle_t. \tag{A3}$$

Note that in Eq. (A3)$\langle \dots \rangle_t$ indicates the time average. We may further define the time-averaged static structure factor $S(\boldsymbol{q}) \equiv N^{-1}\langle \rho(-\boldsymbol{q}, t)\rho(\boldsymbol{q}, t)\rangle_t$, and it is customary to define the normalized time-averaged, lag-time–dependent ISF as

$$\begin{aligned} f(\boldsymbol{q}, \Delta t) &\equiv \langle F(\boldsymbol{q}, \Delta t)\rangle_t / S(\boldsymbol{q}) \\ &= f_{\mathrm{s}}(\boldsymbol{q}, \Delta t) + f_{\mathrm{d}}(\boldsymbol{q}, \Delta t), \end{aligned} \tag{A4}$$

which is referred to as the ISF throughout this study.

2. The DDM Observable

As motivated earlier, instead of considering number densities $\rho(\boldsymbol{x}, t)$, (bright-field) DDM employs intensity maps (i.e., images) of spatially extended objects. For a perfect imaging system, the two-dimensional intensity map in the focal plane ($z = 0$) can be expressed as

$$I(\boldsymbol{x}, t) = \mathcal{T}(\boldsymbol{x}, z) \circledast I_{\mathrm{obj}}(\boldsymbol{x}, z, t)\big|_{z=0} + \xi(\boldsymbol{x}, t), \tag{A5}$$

where $\circledast$ indicates a convolution operation in space, z is the Cartesian coordinate corresponding to the optical axis, $\mathcal{T}(\boldsymbol{x}, z)$ is the transfer function or point-spread function of the imaging system, $I_{\mathrm{obj}}(\boldsymbol{x}, z, t)$ refers to the sample intensity, and $\xi(\boldsymbol{x}, t)$ denotes the camera noise [27]. In our case, digital images of microscopic objects are acquired by a CMOS sensor, using a microscope featuring a quasi-monochromatic, partially incoherent light source and plane wave illumination (i.e., Köhler illumination).

In this study, we are dealing with a complex, scattering, and absorbing sample. Following the derivation of [92], the object intensity in the focal plane is given by

$$I_{\mathrm{obj}}(\boldsymbol{x}, z = 0, t) = \langle I_0\rangle T(\boldsymbol{x}, t), \tag{A6}$$

where $\langle I_0\rangle$ is the spatially averaged intensity of the partially incoherent light source and $T(\boldsymbol{x}, t)$ refers to the (time-dependent) optical transmittance of the sample, which is connected to the imaginary part of the complex refractive index $\tilde{n} = n + ik$ by the Lambert-Beer law. The transmittance of the sample is, however, not the only optical contribution to the intensity detected. Since our sample (i.e., water + biomolecular solutes) is distributed within the imaging chamber along the optical axis, we must consider out-of-focus contributions to the object intensity, as motivated in [92]. These out-of-focus contributions are caused by the finite, non-zero depth of field of the objective lens and scale with the optical transmittance of the sample $T(\boldsymbol{x}, t)$, as well as the lateral optical phase delay gradient $\nabla\phi(\boldsymbol{x}, t)$, which can be motivated by considering

$$\frac{\partial}{\partial z} I_{\mathrm{obj}}(\boldsymbol{x}, z, t)\bigg|_{z=0} = -\langle I_0\rangle \nabla\cdot\left[T(\boldsymbol{x}, t)\nabla\phi(\boldsymbol{x}, t)\right], \tag{A7}$$

assuming a homogeneous, symmetric, and incoherent illumination [92]. In Eq. (A7), $\nabla \equiv (\partial/\partial x, \partial/\partial y)^{\mathrm{T}}$ is the 2D nabla operator in Cartesian coordinates, and the optical phase delay is given by

$$\phi(\boldsymbol{x}, t) = \frac{2\pi}{\lambda}\int_0^{l(\boldsymbol{x})} \mathrm{d}z\, \left(n_{\mathrm{obj}}(\boldsymbol{x}, z, t) - n_0\right), \tag{A8}$$

with λ as the wavelength (distribution) of the light source, $l(\boldsymbol{x})$ denotes the height of the object (in our case, $l = 400\,\mu\text{m}$), n_0 is the refractive index of the surrounding medium (i.e., water), and $n_{\text{obj}}(\boldsymbol{x}, z, t)$ refers to the refractive indices of solutes in the sample, which can be approximated by the Biot equation [93] as $n_{\text{obj}}(\boldsymbol{x}, z, t) = \sum_k v_k(\boldsymbol{x}, z, t)/v_0 n_k$, where v_k/v_0 is the volume fraction of a voxel occupied by species k and n_k is its refractive index. Note that for water-based samples, we have $\phi \geq 0$, i.e., $n_{\text{obj}} \geq n_0$. In this interpretation, the experimental space and time should be treated as discrete variables, i.e., the total volume of the imaging chamber consists of $v = N_v v_0$ voxels with volume v_0 and the measurement time is $t = N_t \delta t$, i.e., N_t frames acquired at a rate $1/\delta t$.

Following the seminal works of [26, 27, 87], we can find an effective, contrast-dependent description of the dynamical evolution of the system under study by considering image differences in terms of a lag time Δt as

$$\begin{aligned} D(\boldsymbol{q}, \Delta t) &\equiv \left\langle |I(\boldsymbol{q}, t + \Delta t) - I(\boldsymbol{q}, t)|^2 \right\rangle_t \\ &\equiv \left[\hat{A}(\boldsymbol{q}) + B(\boldsymbol{q})\right] \left\{1 - \Re\left[f(\boldsymbol{q}, \Delta t)\right]\right\} + B(\boldsymbol{q}). \end{aligned} \tag{A9}$$

where we identify the real part of the normalized ISF $\Re\left[f(\boldsymbol{q}, \Delta t)\right]$ and define the amplitude term $\hat{A}(\boldsymbol{q}) \propto \mathcal{T}(\boldsymbol{q}) S(\boldsymbol{q})$ and the background term $B(\boldsymbol{q}) = \sigma_0^2(\boldsymbol{q})$. Here, we used the assumption that $I(\boldsymbol{q}, t) \propto \rho(\boldsymbol{q}, t)$, and that our camera exhibits delta-correlated noise $\langle \xi(\boldsymbol{x}, t) \xi(\boldsymbol{x}, t + \Delta t) \rangle = \sigma_0^2(\boldsymbol{x}) \delta(\Delta t)$, where $\sigma_0(\boldsymbol{x})$ denotes the standard deviation of the respective noise process of each pixel. For additional information and in-depth discussion, see also [87].

For systems that exhibit isotropic dynamics, Eq. (A9) may be simplified by taking the azimuthal average over the displacement modes $q = |\boldsymbol{q}|$, which resembles the ensemble average over different configurations. Both time and space averaging procedures drastically increase the signal-to-noise ratio of the data.

We note that, considering the concepts introduced above, finding a good (analytical) approximation for the intensity distribution of complex biological systems, such as the cytoplasm (comprising different macromolecular species with specific opacities o_k and refractive indices n_k), is well beyond this study and renders inferences about, as well as simulations of, hypothesized inherent statistical processes a challenging endeavor.

Appendix B: Super-statistical Models

In this appendix, we introduce the theoretical ISF models that are based on super-statistical arguments, following the ideas and results of [43, 59, 62]. The main conclusions of this appendix are summarized in Fig. B1.

1. Fractional Brownian Motion with a Distribution of Diffusivities

a. *Exponential Distribution of Diffusivities*

Following the derivations and results presented in [43], in complex biological matter, one may assume that the diffusivity of similarly sized scatterers is dependent on their position, due to local changes in crowdedness. In this scenario, some tracers could be 'stuck', others might be slowed down, while another fraction moves freely. A statistical distribution that describes these cases in a continuous limit is the exponential distribution, whose probability density function (PDF) is given by

$$\mathcal{E}(x \geq 0; \lambda > 0) \equiv \lambda \exp\left(-\lambda x\right), \tag{B1}$$

where x is the ordinate and λ is the characteristic parameter. Using Eq. (3) for Eq. (B1), one obtains a new PDF of particle displacements:

$$G_{\mathcal{E}}^{\alpha}(\Delta r, \Delta t) = \sqrt{\frac{\lambda}{4\left(\Delta t\right)^{\alpha}}} \exp\left[-\Delta r \sqrt{\frac{\lambda}{\left(\Delta t\right)^{\alpha}}}\right], \tag{B2}$$

which is exactly the PDF of a Laplace distribution $\mathcal{L}\left(\Delta r; \mu = 0, \sigma = \sqrt{\lambda^{-1}\left(\Delta t\right)^{\alpha}}\right)$. The ISF of this process is accordingly given by

$$f_{\mathcal{E}}^{\alpha}(q, \Delta t) = \frac{1}{1 + q^2 \lambda^{-1}\left(\Delta t\right)^{\alpha}}. \tag{B3}$$

For the case of $\lambda = \langle K_\alpha \rangle^{-1}$ we recover Eq. (5).

b. *Inverse Gaussian Distribution of Diffusivities*

Another approach to describing inhomogeneities of complex biological matter, especially in the context of DDM, is based on the idea of a heterogeneous scatterer population, e.g., particles with different sizes. For the Brownian case ($\alpha = 1$), assuming a constant viscosity of the system and considering the Stokes–Einstein relation, it is clear that an exponential distribution of diffusivities is not physical for the case $K \to 0 \Leftrightarrow R \to \infty$, for which the PDF of the exponential distribution yields a finite value $\mathcal{E}\left(K = 0; \lambda = 1/\langle K \rangle\right) = 1/\langle K \rangle$. One potential distribution of diffusivities that fulfills this criterion, however, is given by the inverse Gaussian distribution, whose PDF reads

$$\text{IG}(x > 0; \mu, \sigma) \equiv \sqrt{\frac{\sigma}{2\pi x^3}} \exp\left[-\frac{\sigma\left(x - \mu\right)^2}{2x\mu^2}\right], \tag{B4}$$

with mode

$$\hat{\mu} = -\frac{3\mu^2}{2\sigma} + \frac{\sqrt{9\mu^4 + 4\mu^2\sigma^2}}{2\sigma}. \tag{B5}$$

Interestingly, the inverse Gaussian distribution arises naturally from the first passage time problem of a Brownian motion (with drift). Following the approach outlined above, the new PDF of particle displacements follows the form

$$G_{\mathrm{IG}}(\Delta r, \Delta t) = \frac{\sigma \exp(\sigma/\mu)}{\pi\mu\sqrt{\sigma\Delta t + (\Delta r)^2}} \times \mathcal{K}_1\left[\frac{1}{\mu\Delta t}\sqrt{\sigma\Delta t + (\Delta r)^2}\right], \tag{B6}$$

where $\mathcal{K}_n(z)$ denotes the modified Bessel function of the second kind, which satisfies the differential equation $z^2y'' + zy' - (z^2 + n^2)\, y = 0$ [88]. Computing the Fourier transform of Eq. (B6) with respect to Δr, one obtains

$$f_{\mathrm{IG}}(q, \Delta t) = \exp\left[\sigma/\mu - \sqrt{\sigma^2/\mu^2 + 2q^2\sigma\Delta t}\right]. \tag{B7}$$

For the case of $\mu = \sigma$ (in analogy to the exponential distribution), Eq. (B7) reduces to

$$f_{\mathrm{IG}}(q, \Delta t) = \exp\left[1 - \sqrt{1 + 2q^2\mu\Delta t}\right]. \tag{B8}$$

At this point, the argument about a size distribution of the scatterers holds only for a purely viscous and sufficiently dilute system. Accounting also for potential viscoelastic effects in terms of a fractional Brownian motion is not trivial since there exists no general relationship between the friction term γ_α and the particle radius R for the generalized Stokes–Einstein relation $K_\alpha = k_{\mathrm{B}}\vartheta/\gamma_\alpha m$, where ϑ denotes the temperature and m is the mass of the particle. The precise relationship between K_α and R highly depends on the system properties. However, in a naive attempt to account for a size distribution of particles performing viscoelastic subdiffusion, we employ the following relation

$$K_\alpha = k_{\mathrm{B}}\vartheta/6\pi\eta_\alpha R, \tag{B9}$$

where η_α is the 'fractional' viscosity with dimension $[\eta_\alpha] = \mathrm{mPa\,s}^\alpha$. Using Eq. (B9) we may write Eq. (B8) as

$$f^{\alpha}_{\mathrm{IG}}(q, \Delta t) = \exp\left[1 - \sqrt{1 + 2q^2\langle K_\alpha\rangle(\Delta t)^\alpha}\right], \tag{B10}$$

and connect the non-Gaussianity to a size distribution of particles.

c. *Gamma Distribution of Diffusivities*

Analogously to the reasoning provided above for the choice of an inverse Gaussian distribution of diffusivities, we may develop the superstatistical expression of the ISF for the gamma distribution. The PDF of the gamma distribution is given by

$$\gamma(x > 0; \mu, \nu) = \frac{\nu^{-\mu}}{\Gamma(\mu)} \exp(-x/\nu)\, x^{-1+\mu}, \tag{B11}$$

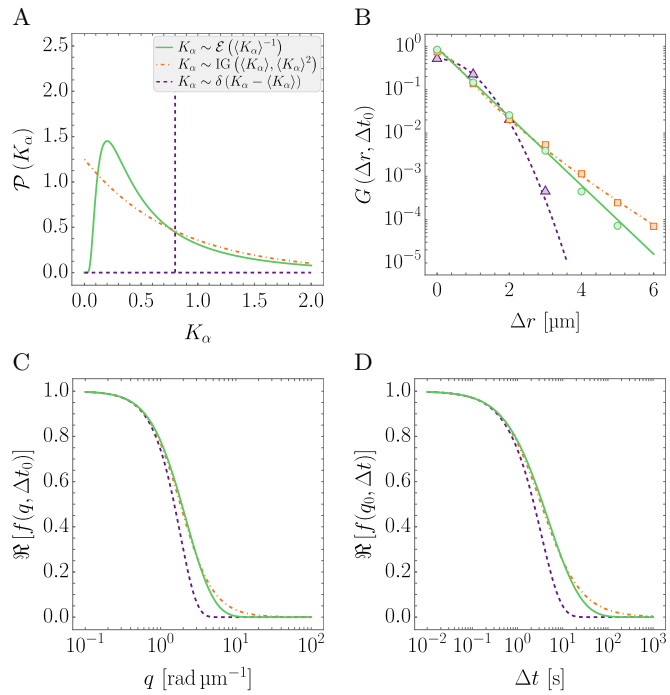

FIG. B1: Results of superstatistical analysis of fractional Brownian motion for different diffusivity distributions with mean $\langle K_\alpha\rangle$ and the fractional scaling exponent α; A: PDFs of diffusivity distributions $\mathcal{P}(K_\alpha)$: exponential distribution Eq. (B1) (orange, dot-dashed), inverse Gaussian distribution Eq. (B4) (green, solid), and delta distribution (purple, dashed). B: Displacement distributions for the cases shown in A at a fixed lag time. The markers indicate MC simulation results and the lines are analytical results (see main text). C and D: Real part of the self-part of the intermediate scattering function for the different cases shown in A in terms of lag time Δt and displacement mode q, respectively.

where μ and ν denote the shape and scale parameters, respectively, and $\Gamma(\dots)$ is the gamma function. The corresponding ISF is then

$$f^{\alpha}_{\gamma}(q, \Delta t) = \left[1 + q^2\nu(\Delta t)^\alpha\right]^{-\mu}. \tag{B12}$$

For $\mu = 1$ and $\nu = \lambda^{-1}$ we recover the Laplacian case Eq. (B3).

The results of the DDM analysis of MC simulations of the super-statistical diffusion scenarios described above are depicted in Fig. B2 and Table B1.

2. Two-State Processes

Following the derivations of [74, 94], we may express a two-state process that consists of two fBm processes with average diffusivities $\langle K_\alpha\rangle, \langle K_\beta\rangle$ and fractional exponents

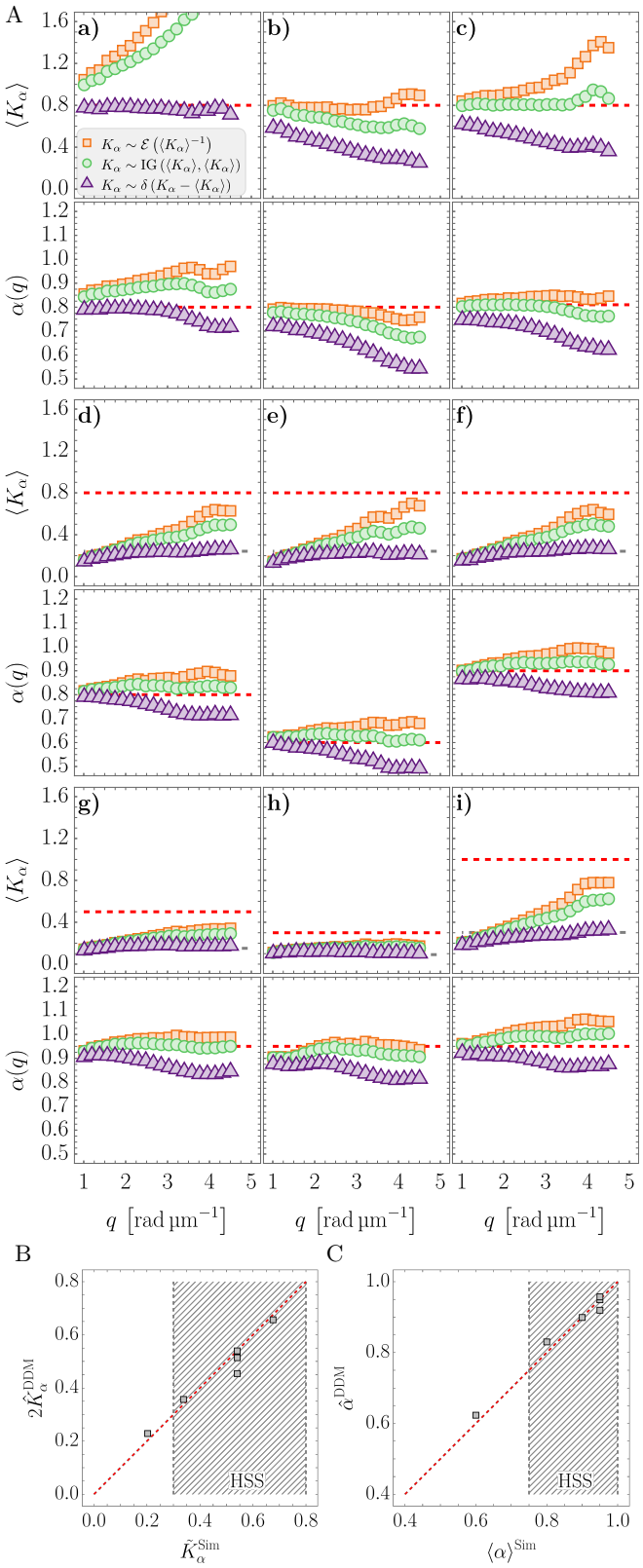

FIG. B2: DDM analysis results of the simulation paradigms depicted in Table B1; A: fractional diffusivity $\langle K_\alpha \rangle$ and fractional exponent α in dependence on the displacement mode q, where the red dashed lines indicate the simulation input. B and C: Comparison of our best estimates from the DDM analysis of cases **d)**–**i)**, $\hat{K}_\alpha^{\mathrm{DDM}}$ and $\hat{\alpha}^{\mathrm{DDM}}$, with the simulation inputs, i.e., the median of the IG diffusivity distribution $\tilde{K}_\alpha^{\mathrm{Sim}}$ and $\langle \alpha \rangle^{\mathrm{Sim}}$. The hatched areas indicate experimentally meaningful parameter ranges of HSS.

	α	$\mathcal{P}(K_\alpha)$	$\langle K_\alpha \rangle$	R [µm]
a)	0.8	$\delta(K_\alpha - \langle K_\alpha \rangle)$	0.8	0.44
b)	0.8	$\mathcal{E}(\langle K_\alpha \rangle^{-1})$	0.8	0.44
c)	0.8	$\mathrm{IG}(\langle K_\alpha \rangle, \langle K_\alpha \rangle)$	0.8	0.44
d)	0.8	$\mathrm{IG}(\langle K_\alpha \rangle, \langle K_\alpha \rangle)$	0.8	$\sim 1/K_\alpha$
e)	0.6	$\mathrm{IG}(\langle K_\alpha \rangle, \langle K_\alpha \rangle)$	0.8	$\sim 1/K_\alpha$
f)	0.9	$\mathrm{IG}(\langle K_\alpha \rangle, \langle K_\alpha \rangle)$	0.8	$\sim 1/K_\alpha$
g)	0.95	$\mathrm{IG}(\langle K_\alpha \rangle, \langle K_\alpha \rangle)$	0.5	$\sim 1/K_\alpha$
h)	0.95	$\mathrm{IG}(\langle K_\alpha \rangle, \langle K_\alpha \rangle)$	0.3	$\sim 1/K_\alpha$
i)	0.95	$\mathrm{IG}(\langle K_\alpha \rangle, \langle K_\alpha \rangle)$	1.0	$\sim 1/K_\alpha$

TABLE B1: Overview of the different numerical simulation schemes performed in this study (see Section IV G and the main text for further information). In cases **a)**–**c)**, the scatterers follow a fractional diffusivity distribution $\mathcal{P}(K_\alpha)$ while their radii R are the same. For cases **d)**–**i)**, the scatterers follow a fractional diffusivity distribution $\mathcal{P}(K_\alpha)$ and their radii are calculated using a generalized Stokes–Einstein relation Eq. (B9), with $\vartheta = 23°\mathrm{C}$ and a constant 'fractional' viscosity $\eta_\alpha = 1\,\mathrm{mPa\,s}^\alpha$. The corresponding results of the DDM analysis are displayed in Fig. B2.

α, β as

$$f_\delta^{\alpha\beta}(q, \Delta t) = \varphi(q) \exp\left[-q^2 \langle K_\alpha \rangle (\Delta t)^\alpha\right] + (1 - \varphi(q)) \exp\left[-q^2 \langle K_\beta \rangle (\Delta t)^\beta\right], \tag{B13}$$

where $\varphi(q)$ is the occupation or volume fraction of particles that follow the α process, and, consistently, $1 - \varphi(q)$ is the occupation or volume fraction of particles that follow the β process.

To examine the applicability of Eq. (B13), we consider the following freeze-in scenario. In this scenario, we employ an IG distribution of diffusivities $K \sim \mathrm{IG}(\langle K \rangle, \langle K \rangle)$ with a corresponding size of scatterers, as described above, and define a cutoff K^*, such that

$$\int_0^{K^*} \mathrm{d}K\, \mathrm{IG}(K; \langle K \rangle, \langle K \rangle) = p. \tag{B14}$$

This cutoff defines two diffusivity populations: $K \to K_\alpha$ for $K \geq K^*$, i.e., smaller scatterers, and $K \to K_\beta$ for $K < K^*$, i.e., larger scatterers. The freeze-in mechanism is then captured by slowing the diffusivity of the β-process down by tenfold, $K_\beta \to K_\beta/10$, and assigning $\beta \to 0.6$, whereas for the α-process, no changes occur. In this model, p effectively tunes the length scale of the freeze-in mechanism.

The results of the DDM analysis of the freeze-in scenario MC simulations described above are depicted in Fig. B3 and Fig. B4.

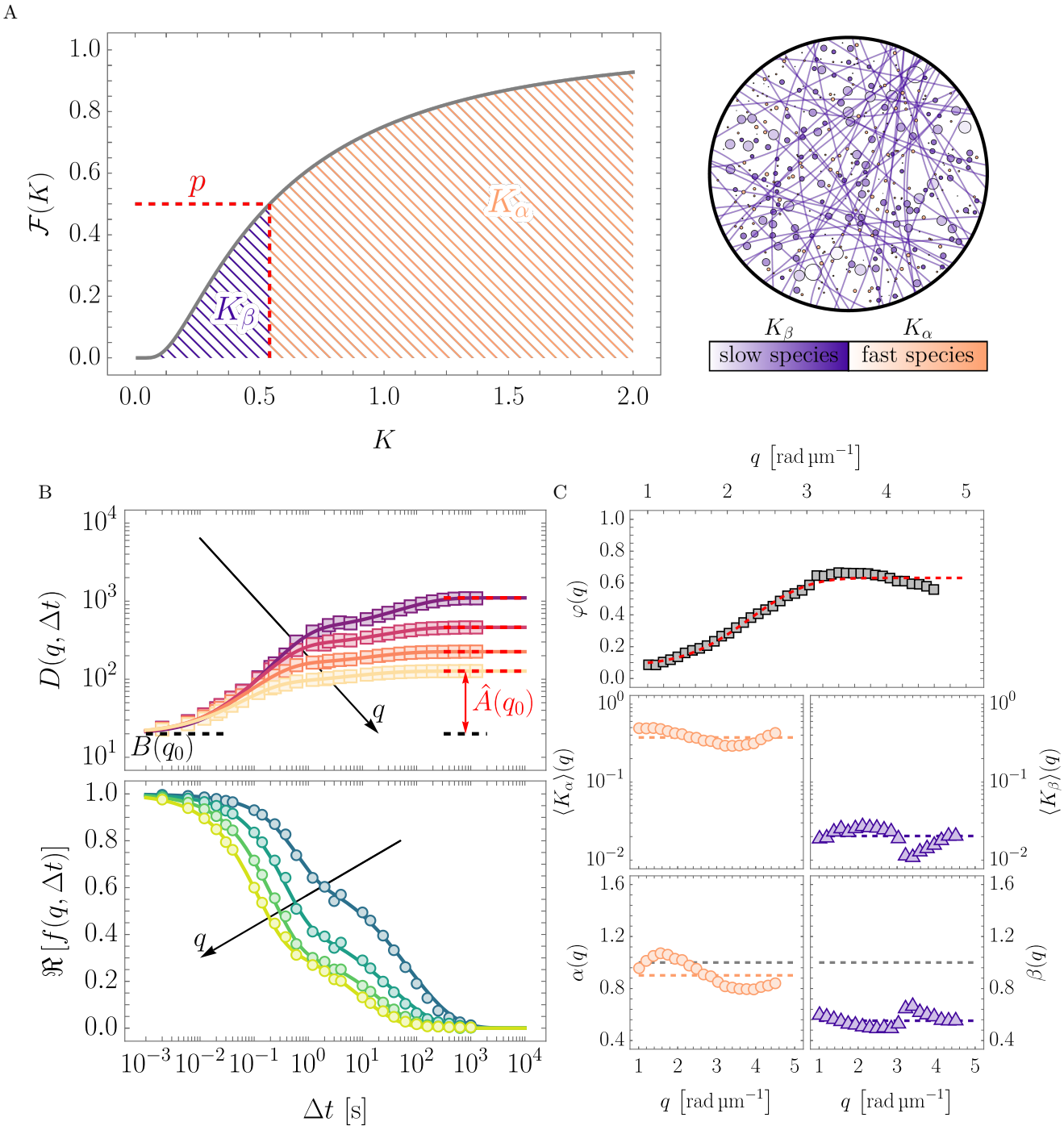

FIG. B3: Overview and results of the two-state process simulation scheme described in the main text; A left: Cumulative distribution function of diffusivities $\mathcal{F}(K)$ of the inverse Gaussian distribution IG $(\langle K\rangle, \langle K\rangle)$ for $\langle K\rangle = 0.8\,\mu\text{m}^2/\text{s}$ (solid gray line) and the probability p that defines the cutoff diffusivity K^* (red dashed line) which is used to define $K \to K_\alpha$ for $K \geq K^*$ and $K \to K_\beta/10$ for $K < K^*$ with the respective fractional exponents α and β. A right: Schematic display of the simulated system, where the orange disks indicate the 'fast species' corresponding to the fractional Brownian motion process with diffusivity distribution $K \sim K_\alpha$ and fractional exponent α and the 'slow species' indicated by the purple disks and streaks corresponding to the fractional Brownian motion process with diffusivity distribution $K \sim K_\beta$ and fractional exponent β. B: DDM results of a simulation of the two-state process depicted in A for the case of $p = 0.2$ in analogy of Fig. 3; top: DDM observable $D(q, \Delta t)$ and bottom: real part of the ISF $\Re\,[f\,(q, \Delta t)]$ (circles) and fits of the ISF using Eq. (11). C: Fitting parameters of the data shown in B as a function of the displacement mode q; top: mixing parameter φ where the red dashed line indicates the best fit to the data with a stretched sigmoidal function denoted in the inset at the top, middle: diffusivities K_α (orange circles) and K_β (purple up-triangles) where the dashed lines indicate the median values of the data, and bottom: fractional exponents α (orange circles) and β (purple up-triangles) where the colorful dashed lines indicate the median of the data and the gray dashed lines indicate $\alpha = \beta = 1$.

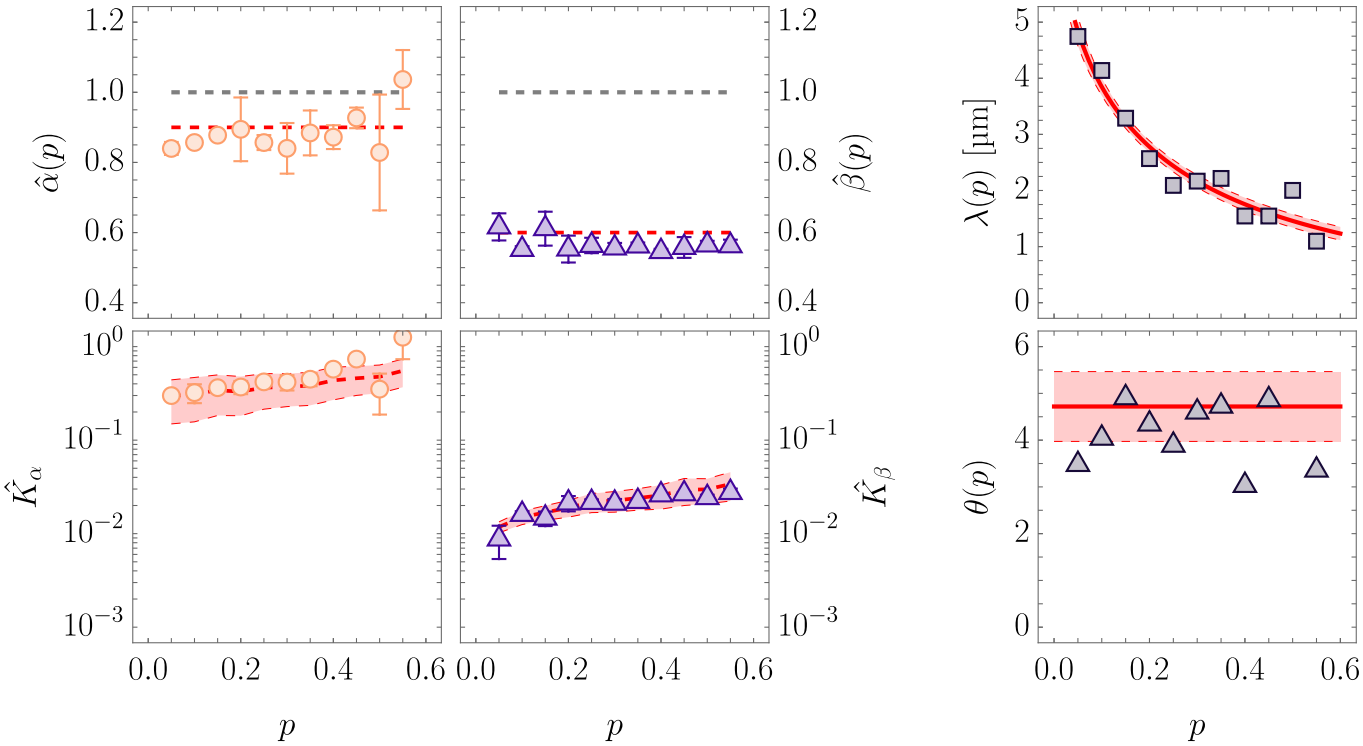

FIG. B4: Results overview of the two-state simulation paradigm described in Appendix B 2 and shown in Fig. B3; left: fractional diffusivity estimates $\hat{K}_\alpha$ and $\hat{K}_\beta$ (top row) and fractional exponent estimates $\hat{\alpha}$ and $\hat{\beta}$ (bottom row) as a function of the cutoff probability p, where the red dashed lines indicate the simulation input values (median with 68% CI) and the gray dashed lines for the fractional exponents indicate $\alpha = \beta = 1$. Right: Fitting results of $\varphi(q)$ with Eq. (12) over the cutoff probability p; characteristic length scale λ (top) and scaling exponent θ (bottom), where the red lines indicate best fit estimates with 68% CIs.

REFERENCES

[1] R. P. Sear, The cytoplasm of living cells: a functional mixture of thousands of components, Journal of Physics: Condensed Matter **17**, S3587 (2005).

[2] S. Shamipour, S. Caballero-Mancebo, and C.-P. Heisenberg, Cytoplasm's got moves, Developmental Cell **56**, 213 (2021).

[3] B. R. Parry, I. V. Surovtsev, M. T. Cabeen, C. S. O'Hern, E. R. Dufresne, and C. Jacobs-Wagner, The bacterial cytoplasm has glass-like properties and is fluidized by metabolic activity, Cell **156**, 183 (2014).

[4] A. T. Molines, J. Lemière, M. Gazzola, I. E. Steinmark, C. H. Edrington, C.-T. Hsu, P. Real-Calderon, K. Suhling, G. Goshima, L. J. Holt, M. Thery, G. J. Brouhard, and F. Chang, Physical properties of the cytoplasm modulate the rates of microtubule polymerization and depolymerization, Developmental Cell **57**, 466 (2022).

[5] A. A. Choi, C. Y. Zhou, A. Tabo, R. Heald, and K. Xu, Single-molecule diffusivity quantification in *Xenopus* egg extracts elucidates physicochemical properties of the cytoplasm, Proceedings of the National Academy of Sciences **121**, e2411402121 (2024).

[6] X. Cheng and J. E. Ferrell, Spontaneous emergence of cell-like organization in *Xenopus* egg extracts, Science **366**, 631 (2019).

[7] A. C. Groen, M. Coughlin, and T. J. Mitchison, Microtubule assembly in meiotic extract requires glycogen, Molecular Biology of the Cell **22**, 3139 (2011).

[8] C. Alfano, Y. Fichou, K. Huber, M. Weiss, E. Spruijt, S. Ebbinghaus, G. De Luca, M. A. Morando, V. Vetri, P. A. Temussi, and A. Pastore, Molecular crowding: The history and development of a scientific paradigm, Chemical Reviews **124**, 3186 (2024).

[9] D. S. Banks and C. Fradin, Anomalous diffusion of proteins due to molecular crowding, Biophysical Journal **89**, 2960 (2005).

[10] D. E. Discher, P. Janmey, and Y. li Wang, Tissue cells feel and respond to the stiffness of their substrate, Science **310**, 1139 (2005).

[11] A. J. Engler, S. Sen, H. L. Sweeney, and D. E. Discher, Matrix elasticity directs stem cell lineage specification, Cell **126**, 677 (2006).

[12] J. Swift, I. L. Ivanovska, A. Buxboim, T. Harada, P. C. D. P. Dingal, J. Pinter, J. D. Pajerowski, K. R. Spinler, J.-W. Shin, M. Tewari, F. Rehfeldt, D. W. Speicher, and D. E. Discher, Nuclear lamin-a scales with tissue stiffness and enhances matrix-directed differentiation, Science **341**, 1240104 (2013).

[13] F. Höfling and T. Franosch, Anomalous transport in the crowded world of biological cells, Reports on Progress in Physics **76**, 046602 (2013).

[14] P.-Y. Gires, M. Thampi, S. W. Krauss, and M. Weiss, Exploring generic principles of compartmentalization in a developmental in vitro model, Development **150**, dev200851 (2023).

[15] A. J. Ford and P. Rajagopalan, Measuring cytoplasmic stiffness of fibroblasts as a function of location and substrate rigidity using atomic force microscopy, ACS Biomaterials Science & Engineering **4**, 3974 (2018), pMID: 33418798.

[16] I. Golding and E. C. Cox, Physical nature of bacterial cytoplasm, Phys. Rev. Lett. **96**, 098102 (2006).

[17] D. Wirtz, Particle-tracking microrheology of living cells: Principles and applications, Annual Review of Biophysics **38**, 301 (2009).

[18] T. M. Muenker, B. E. Vos, and T. Betz, Intracellular mechanical fingerprint reveals cell type specific mechanical tuning, eLife 10.7554/elife.97416.1 (2024).

[19] J. Ries and P. Schwille, Fluorescence correlation spectroscopy, BioEssays **34**, 361 (2012).

[20] T. Ohrt, J. Mütze, W. Staroske, L. Weinmann, J. Höck, K. Crell, G. Meister, and P. Schwille, Fluorescence correlation spectroscopy and fluorescence cross-correlation spectroscopy reveal the cytoplasmic origination of loaded nuclear risc in vivo in human cells, Nucleic Acids Research **36**, 6439 (2008).

[21] W. Y. C. Huang, X. Cheng, and J. E. Ferrell, Cytoplasmic organization promotes protein diffusion in xenopus extracts, Nature Communications **13**, 5599 (2022).

[22] K. Wang, X. H. Sun, Y. Zhang, T. Zhang, Y. Zheng, Y. C. Wei, P. Zhao, D. Y. Chen, H. A. Wu, W. H. Wang, R. Long, J. B. Wang, and J. Chen, Characterization of cytoplasmic viscosity of hundreds of single tumour cells based on micropipette aspiration, Royal Society Open Science **6**, 181707 (2019).

[23] R. M. Hochmuth, Micropipette aspiration of living cells, Journal of Biomechanics **33**, 15 (2000).

[24] Y. Hao, S. Cheng, Y. Tanaka, Y. Hosokawa, Y. Yalikun, and M. Li, Mechanical properties of single cells: Measurement methods and applications, Biotechnology Advances **45**, 107648 (2020).

[25] P.-H. Wu, D. R.-B. Aroush, A. Asnacios, W.-C. Chen, M. E. Dokukin, B. L. Doss, P. Durand-Smet, A. Ekpenyong, J. Guck, N. V. Guz, P. A. Janmey, J. S. H. Lee, N. M. Moore, A. Ott, Y.-C. Poh, R. Ros, M. Sander, I. Sokolov, J. R. Staunton, N. Wang, G. Whyte, and D. Wirtz, A comparison of methods to assess cell mechanical properties, Nature Methods **15**, 10.1038/s41592-018-0015-1 (2018).

[26] R. Cerbino and V. Trappe, Differential dynamic microscopy: Probing wave vector dependent dynamics with a microscope, Phys. Rev. Lett. **100**, 188102 (2008), 1507.01344.

[27] P. Edera, D. Bergamini, V. Trappe, F. Giavazzi, and R. Cerbino, Differential dynamic microscopy microrheology of soft materials: A tracking-free determination of the frequency-dependent loss and storage moduli, Phys. Rev. Mater. **1**, 073804 (2017), 1708.07170.

[28] M. Drechsler, F. Giavazzi, R. Cerbino, and I. M. Palacios, Active diffusion and advection in drosophila oocytes result from the interplay of actin and microtubules, Nature Communications **8**, 1520 (2017).

[29] D. Germain, M. Leocmach, and T. Gibaud, Differential dynamic microscopy to characterize brownian motion and bacteria motility, American Journal of Physics **84**, 202 (2016), 1511.00923.

[30] V. A. Martinez, R. Besseling, O. A. Croze, J. Tailleur, M. Reufer, J. Schwarz-Linek, L. G. Wilson, M. A. Bees, and W. C. K. Poon, Differential dynamic microscopy: A high-throughput method for characterizing the motility of microorganisms, Biophysical Journal **103**, 1637 (2012), 1202.1702.

[31] M. Al-Shahrani and G. Bryant, Differential dynamic microscopy for the characterisation of motility in biological systems, Phys. Chem. Chem. Phys. **24**, 20616 (2022).

[32] H. N. Verwei, G. Lee, G. Leech, I. I. Petitjean, G. H.

Koenderink, R. M. Robertson-Anderson, and R. J. McGorty, Quantifying cytoskeleton dynamics using differential dynamic microscopy, JoVE , e63931 (2022).

[33] S. J. Anderson, J. Garamella, S. Adalbert, R. J. McGorty, and R. M. Robertson-Anderson, Subtle changes in crosslinking drive diverse anomalous transport characteristics in actin–microtubule networks, Soft Matter **17**, 4375 (2021).

[34] C. Guidolin, C. Heim, N. B. P. Adams, P. Baaske, V. Rondelli, R. Cerbino, and F. Giavazzi, Protein sizing with differential dynamic microscopy, Macromolecules **56**, 8290 (2023), 2307.12608.

[35] S. Hanio, S. Möllmert, C. Möckel, S. Choudhury, A. I. Höpfel, T. Zorn, S. Endres, J. Schlauersbach, L. Scheller, C. Keßler, O. Scherf-Clavel, P. Bellstedt, U. S. Schubert, A.-C. Pöppler, K. G. Heinze, J. Guck, and L. Meinel, Bile is a selective elevator for mucosal mechanics and transport, Molecular Pharmaceutics **20**, 6151 (2023).

[36] F. Ling, A. T. Sahin, B. Miller Naranjo, S. Aime, D. Roth, N. Tepho, A. S. Vendrame, E. Emken, M. Kiechle, Y. Tesfaigzi, O. Lieleg, and J. Nawroth, High-throughput mucus microrheology for phenotyping and disease modeling, bioRxiv , 2025.01.09.632077 (2025).

[37] R. Cerbino and P. Cicuta, Perspective: Differential dynamic microscopy extracts multi-scale activity in complex fluids and biological systems, The Journal of Chemical Physics **147**, 110901 (2017).

[38] L. Van Hove, Correlations in space and time and born approximation scattering in systems of interacting particles, Phys. Rev. **95**, 249 (1954).

[39] A. Biswas, K. Kim, G. Cojoc, J. Guck, and S. Reber, The *Xenopus* spindle is as dense as the surrounding cytoplasm, Developmental Cell **56**, 967 (2021).

[40] R. Metzler, Gaussianity fair: The riddle of anomalous yet non-gaussian diffusion, Biophysical Journal **112**, 413 (2017).

[41] B. Wang, J. Kuo, S. C. Bae, and S. Granick, When brownian diffusion is not gaussian, Nature Materials **11**, 481 (2012).

[42] T. A. Waigh and N. Korabel, Heterogeneous anomalous transport in cellular and molecular biology, Reports on Progress in Physics **86**, 126601 (2023).

[43] T. J. Lampo, S. Stylianidou, M. P. Backlund, P. A. Wiggins, and A. J. Spakowitz, Cytoplasmic rna-protein particles exhibit non-gaussian subdiffusive behavior, Biophysical Journal **112**, 532 (2017).

[44] M. C. Munder, D. Midtvedt, T. Franzmann, E. Nüske, O. Otto, M. Herbig, E. Ulbricht, P. Müller, A. Taubenberger, S. Maharana, L. Malinovska, D. Richter, J. Guck, V. Zaburdaev, and S. Alberti, A ph-driven transition of the cytoplasm from a fluid- to a solid-like state promotes entry into dormancy, eLife **5**, e09347 (2016).

[45] J.-H. Jeon, M. Javanainen, H. Martinez-Seara, R. Metzler, and I. Vattulainen, Protein crowding in lipid bilayers gives rise to non-gaussian anomalous lateral diffusion of phospholipids and proteins, Phys. Rev. X **6**, 021006 (2016).

[46] M. Wühr, R. M. Freeman, M. Presler, M. E. Horb, L. Peshkin, S. P. Gygi, and M. W. Kirschner, Deep proteomics of the xenopus laevis egg using an mrna-derived reference database, Current Biology **24**, 1467 (2014).

[47] D. A. Fletcher and R. D. Mullins, Cell mechanics and the cytoskeleton, Nature **463**, 485 (2010).

[48] M. N. Starodubtseva, Mechanical properties of cells and ageing, Ageing Research Reviews **10**, 16 (2011), cell Motility and Ageing.

[49] A. Massey, J. Stewart, C. Smith, C. Parvini, M. McCormick, K. Do, and A. X. Cartagena-Rivera, Mechanical properties of human tumour tissues and their implications for cancer development, Nature Reviews Physics **6**, 269 (2024).

[50] W. Deng and E. Barkai, Ergodic properties of fractional brownian-langevin motion, Phys. Rev. E **79**, 011112 (2009), 0809.2430.

[51] R. Metzler, J.-H. Jeon, A. G. Cherstvy, and E. Barkai, Anomalous diffusion models and their properties: non-stationarity, non-ergodicity, and ageing at the centenary of single particle tracking, Phys. Chem. Chem. Phys. **16**, 24128 (2014).

[52] R. Metzler and J. Klafter, Subdiffusive transport close to thermal equilibrium: From the langevin equation to fractional diffusion, Phys. Rev. E **61**, 6308 (2000).

[53] V. Kobelev and E. Romanov, Fractional langevin equation to describe anomalous diffusion, Progress of Theoretical Physics Supplement **139**, 470 (2000), chao-dyn/9908001.

[54] J.-H. Jeon and R. Metzler, Fractional brownian motion and motion governed by the fractional langevin equation in confined geometries, Phys. Rev. E **81**, 021103 (2010).

[55] D. Ernst, M. Hellmann, J. Köhler, and M. Weiss, Fractional brownian motion in crowded fluids, Soft Matter **8**, 4886 (2012).

[56] J. Szymanski and M. Weiss, Elucidating the origin of anomalous diffusion in crowded fluids, Phys. Rev. Lett. **103**, 038102 (2009).

[57] A. Bonfanti, J. L. Kaplan, G. Charras, and A. Kabla, Fractional viscoelastic models for power-law materials, Soft Matter **16**, 6002 (2020), 2003.07834.

[58] C. Beck and E. Cohen, Superstatistics, Physica A: Statistical Mechanics and its Applications **322**, 267 (2003), cond-mat/0205097.

[59] A. V. Chechkin, F. Seno, R. Metzler, and I. M. Sokolov, Brownian yet non-gaussian diffusion: From superstatistics to subordination of diffusing diffusivities, Phys. Rev. X **7**, 021002 (2017), 1611.06202.

[60] M. E. Young, P. A. Carroad, and R. L. Bell, Estimation of diffusion coefficients of proteins, Biotechnology and Bioengineering **22**, 947 (1980).

[61] S. Hapca, J. W. Crawford, and I. M. Young, Anomalous diffusion of heterogeneous populations characterized by normal diffusion at the individual level, Journal of The Royal Society Interface **6**, 111 (2009).

[62] C. Runfola, S. Vitali, and G. Pagnini, The fokker–planck equation of the superstatistical fractional brownian motion with application to passive tracers inside cytoplasm, Royal Society Open Science **9**, 221141 (2022).

[63] M. S. Safari, M. A. Vorontsova, R. Poling-Skutvik, P. G. Vekilov, and J. C. Conrad, Differential dynamic microscopy of weakly scattering and polydisperse protein-rich clusters, Phys. Rev. E **92**, 042712 (2015).

[64] B. J. Frisken, Revisiting the method of cumulants for the analysis of dynamic light-scattering data, Appl. Opt. **40**, 4087 (2001).

[65] E. Raspelli, L. Falbo, and V. Costanzo, Xenopus egg extract to study regulation of genome-wide and locus-specific dna replication, genesis **55**, e22996 (2017).

[66] A. Arango-Restrepo, D. Barragán, and J. M. Rubi, Self-assembling outside equilibrium: emergence of structures

mediated by dissipation, Phys. Chem. Chem. Phys. **21**, 17475 (2019).

[67] A. Singh, P. Parvin, B. Saha, and D. Das, Non-equilibrium self-assembly for living matter-like properties, Nature Reviews Chemistry **8**, 723 (2024).

[68] I. M. Sokolov, Models of anomalous diffusion in crowded environments, Soft Matter **8**, 9043 (2012).

[69] M. Balcerek, S. Thapa, K. Burnecki, H. Kantz, R. Metzler, A. Wyłomańska, and A. Chechkin, Multifractional brownian motion with telegraphic, stochastically varying exponent (2025), arXiv:2504.14546 [cond-mat.stat-mech].

[70] P. J. Foster, S. Fürthauer, M. J. Shelley, D. J. Needleman, and A. Akhmanova, Active contraction of microtubule networks, eLife **4**, e10837 (2015).

[71] P. J. Foster, W. Yan, S. Fürthauer, M. J. Shelley, and D. J. Needleman, Connecting macroscopic dynamics with microscopic properties in active microtubule network contraction, New Journal of Physics **19**, 125011 (2017).

[72] R. Pastore, A. Ciarlo, G. Pesce, A. Sasso, and F. Greco, A model-system of fickian yet non-gaussian diffusion: light patterns in place of complex matter, Soft Matter **18**, 351 (2022).

[73] M. S. Safari, R. Poling-Skutvik, P. G. Vekilov, and J. C. Conrad, Differential dynamic microscopy of bidisperse colloidal suspensions, npj Microgravity **3**, 21 (2017).

[74] C. Dieball, D. Krapf, M. Weiss, and A. Godec, Scattering fingerprints of two-state dynamics, New Journal of Physics **24**, 023004 (2022).

[75] M. Valentine, Z. Perlman, T. Mitchison, and D. Weitz, Mechanical properties of xenopus egg cytoplasmic extracts, Biophysical Journal **88**, 680 (2005).

[76] A. Biswas, O. Muñoz, K. Kim, C. Hoege, B. M. Lorton, D. Shechter, J. Guck, V. Zaburdaev, and S. Reber, Conserved nucleocytoplasmic density homeostasis drives cellular organization across eukaryotes, bioRxiv 10.1101/2023.09.05.556409 (2023).

[77] H. Kim and M. Delarue, Dynamic structure of the cytoplasm, Current Opinion in Cell Biology **94**, 102507 (2025).

[78] K. Speckner and M. Weiss, Single-particle tracking reveals anti-persistent subdiffusion in cell extracts, Entropy **23**, 10.3390/e23070892 (2021).

[79] H. Jiang and S. X. Sun, Cellular pressure and volume regulation and implications for cell mechanics, Biophysical Journal **105**, 609 (2013).

[80] V. Mittelheisser, V. Gensbittel, L. Bonati, W. Li, L. Tang, and J. G. Goetz, Evidence and therapeutic implications of biomechanically regulated immunosurveillance in cancer and other diseases, Nature Nanotechnology **19**, 281 (2024).

[81] T. M. Muenker, G. Knotz, M. Krüger, and T. Betz, Accessing activity and viscoelastic properties of artificial and living systems from passive measurement, Nature Materials **23**, 1283 (2024).

[82] G. Knotz and M. Krüger, Mean back relaxation for position and densities, Phys. Rev. E **110**, 044137 (2024).

[83] S. Cai, Z. Mao, Z. Wang, M. Yin, and G. E. Karniadakis, Physics-informed neural networks (pinns) for fluid mechanics: a review, Acta Mechanica Sinica **37**, 1727 (2021).

[84] S. Reusch, A. Biswas, W. G. Hirst, and S. Reber, Affinity purification of label-free tubulins from xenopus egg extracts, STAR Protocols **1**, 100151 (2020).

[85] C. Bernis and D. J. Forbes, Chapter 8 - analysis of nuclear reconstitution, nuclear envelope assembly, and nuclear pore assembly using xenopus in vitro assays, in *Nuclear Pore Complexes and Nucleocytoplasmic Transport - Methods*, Methods in Cell Biology, Vol. 122, edited by V. Doye (Academic Press, 2014) pp. 165–191.

[86] A. Shkarin, Alexshkarin/pylablib: Update to 1.4.3 (2024).

[87] F. Giavazzi, D. Brogioli, V. Trappe, T. Bellini, and R. Cerbino, Scattering information obtained by optical microscopy: Differential dynamic microscopy and beyond, Phys. Rev. E **80**, 031403 (2009).

[88] W. R. Inc., Mathematica, Version 12.3, champaign, IL, 2024.

[89] F. Giavazzi, P. Edera, P. J. Lu, and R. Cerbino, Image windowing mitigates edge effects in differential dynamic microscopy, The European Physical Journal E **40**, 97 (2017).

[90] F. Giavazzi, S. Crotti, A. Speciale, F. Serra, G. Zanchetta, V. Trappe, M. Buscaglia, T. Bellini, and R. Cerbino, Viscoelasticity of nematic liquid crystals at a glance, Soft Matter **10**, 3938 (2014).

[91] P. Hopkins, A. Fortini, A. J. Archer, and M. Schmidt, The van hove distribution function for brownian hard spheres: Dynamical test particle theory and computer simulations for bulk dynamics, The Journal of Chemical Physics **133**, 224505 (2010), 1010.2124.

[92] N. Streibl, Phase imaging by the transport equation of intensity, Optics Communications **49**, 6 (1984).

[93] C. Möckel, T. Beck, S. Kaliman, S. Abuhattum, K. Kim, J. Kolb, D. Wehner, V. Zaburdaev, and J. Guck, Estimation of the mass density of biological matter from refractive index measurements, Biophysical Reports **4**, 10.1016/j.bpr.2024.100156 (2024).

[94] M. Balcerek, K. Burnecki, S. Thapa, A. Wyłomańska, and A. Chechkin, Fractional brownian motion with random hurst exponent: Accelerating diffusion and persistence transitions, Chaos: An Interdisciplinary Journal of Nonlinear Science **32**, 093114 (2022), 2206.03818.